공학박사 학위논문

Electrochemistry in Oxygen Reductions for Pt-Based Nanoparticles Prepared by Chemical Methods

화학적 방법으로 준비된 백금 기반 나노입자에 대한 산소환원의 전기화학

2013년 8월

서울대학교 대학원

공과대학 화학생물공학부

정 영 훈

Abstract

Electrochemistry in Oxygen Reductions for Pt-Based Nanoparticles Prepared by Chemical Methods

Young-Hoon Chung

School of Chemical & Biological Engineering

Seoul National University

The proton exchange membrane fuel cell (PEMFC) would be potentially suitable as a sustainable power source to substitute fossil fuel for automobiles and portable devices. For commercialization of the PEMFC, the oxygen reduction reaction (ORR) is one of the most significant problems to be overcome due to a considerable high overpotential for Pt, known as the highest electrocatalytic activity of the ORR. According to the theory, the overpotential of the ORR for Pt(111) is originated from the adsorbed oxygen containing species tend to be so stable at near equilibrium potential. As a result, there are many attempts to weaken the adsorption strength onto Pt by modifying the surface d-band structure.

For a practical application, the preparation of Pt-based nanoparticles supported on carbon has been intensively investigated for several decades. To obtain nanoparticles, the nuclei formed from the precursor should be grown slowly. If the growth rates cannot be controlled, the dissolved particles will diffuse toward larger particles and deposit to minimize the surface free energy through a process known as Ostwald ripening. Once Ostwald ripening occurs, the particle size distribution increases. The synthetic environments including,

organic solvents, capping, and reducing agents can be stabilized on the surface of the nanoparticles by lowering the rate of growth through either steric or electrostatic stabilization. However, the capped organic species were strongly adsorbed on the surface of Pt-based nanoparticles resulting in tuning the electrochemical reactions. Considering electrochemistry in the ORR is significantly influenced on the electronic structures, the synthetic environment must be primarily important factors, that is, the preparation stage, as-prepared state, and post-treatment process due to alteration of electronic structure. In this thesis, we investigated the relationship between electrochemistry in oxygen reductions and electronic structure for Pt-based nano-catalysts in accordance with those factors.

Concerning the Pt-based nano-catalysts in the preparation stage, the Pt_1Fe_x (x = 1, 2, and 3) nanoparticles were studied. The aim of this part is primarily on understanding of the effect of the surface composition for the electrocatalytic activity. To clarify this correlation, we compared two types of nanoparticles with the different surface composition, the Fe-rich and the Pt-Fe mixed surface. We synthesized highly dispersed carbon supported Pt_1Fe_x nanoparticles with the Fe-rich surface (~ 2 nm) through a preferential interaction of a capping agent and metal species, *i.e.*, Fe-OOC. Because of the phase separation of Pt and Fe species through the preferential interaction of the capping molecule, the electrocatalytic properties of nanoparticles were not significantly changed despite the various Pt/Fe ratios. Otherwise, nanoparticles with the Pt-Fe mixed surface, prepared by the difference of segregation energy, demonstrated that the electrochemical characteristic were significantly altered due to the interaction between Pt and Fe species on the surface of electrocatalysts. In particular to the ORR, the Pt_1Fe_2 nanoparticle with the Pt-Fe mixed surface showed the highest enhancement for the specific activity compared to Pt, resulting from the development of the stable *fcc* PtFe phase. This result indicates the electrocatalytic activity of the bimetallic

nanoparticles decisively is determined the surface composition rather than the bulk composition.

Next, we scrutinized the as-prepared state of nano-catalysts. Capping organic molecules including oleylamine, strongly adsorbed onto Pt nanoparticles during preparation steps, are considered as an undesirable species for the oxygen reduction reaction due to decreasing electrochemical active sites. However, we found the small amount of oleylamine modified platinum nanoparticles showed the significant enhancement of the electrochemical activity oxygen reduction reaction, even with the loss of electrochemical active surface area. The enhancement was correlated with downshift of frontier d-band structure of platinum and the retardation of competitively adsorbed species. These results suggest that a capping organic molecule modified electrode can be a strategy to design an advanced electrocatalyst by modification of electronic structures.

Finally, we examined how to affect the post-treatment process, *i.e.*, thermal annealing after the preparation of PtNi nanoparticles into the two variation, temperature and atmosphere. Firstly, we explored that the temperature of thermal annealing is how to influence the ORR behaviors. The reconstruction of PtNi nanoparticles, that is, intermetallic ordering and surface reorientation into the (111) facet, were developed by the heat treatment at the different thermal energy without severe agglomeration. The enhancement of electrocatalytic activity was correlated with this structural change. Also, electrochemically stable structure was formed after the reconstruction resulting in increasing intermetallic interaction between Pt and Ni. This result explained how to enhance the ORR properties by the thermal annealing process and proposed the way to design the advanced electrocatalysts. Secondly, the purpose of this part is mainly on tuning the oxygen reduction activity of Pt_2Ni_1 nanoparticles induced by the heat treatment atmosphere. From the observation of the X-ray spectroscopic measurement, it is revealed

that the electronic structures were varied with the heat treatment condition. The argon treated electrocatalyst demonstrated the highest catalytic activity in the half-cell measurement owing to the appropriate electronic interaction between Pt and Ni. This result suggested that the alteration of electronic structures induced by the heat treatment atmosphere was decisively influenced to the ORR activity particularly in the presence of the specific adsorption.

Keywords**:** electrochemistry, electronic structure, fuel cell, nanoparticle, oxygen reduction, platinum
Student Number**:** 2009-31265

Contents

List of Tables

List of Figures

Chapter 1. Introduction

1.1. Fuel cell

1.1.1. Electrochemistry Basics

The electrochemical reaction is one of kinds of the chemical reactions, accompanied with electron transfer through the system. The electrochemical system composes of anode, cathode, electrolyte and external circuit. Involved in the system, electrons should be considered when to analyze the electrochemical reaction. Potential and current are commonly used as basic descriptors of the electrochemical reaction. An electrochemical potential is defined as the sum of the chemical and the electric potential. Therefore, the equilibrium potential can be formulated by the equation, so-called Nernst equation;

$$E_{eq} = E^0 + \frac{nF}{RT}\left(\sum_i \ln a_i^o - \sum_j \ln a_j^R\right)$$

where, E_{eq}, E^o, n, F, R, a^O, and a^R are equilibrium potential, standard potential, number of electrons, Faradaic constant, ideal gas constant, activity of oxidants, and activity of reductants, respectively.

Current, the net flow of the electrons in the system, can be expressed by the sum of the rate of reaction of the anode and the cathode. The equation shows the correlation of the current and the kinetic of reaction.

$$i_{net} = i_0 \left[\frac{C_O(0,t)}{C_O^*} e^{-\frac{\beta nF(E-E_{eq})}{RT}} - \frac{C_R(0,t)}{C_R^*} e^{\frac{(1-\beta)nF(E-E_{eq})}{RT}} \right]$$

where, i_0, β, E, E_{eq}, C_O^*, C_O, C_R^*, and C_R are exchange current, symmetry factor, applied potential, equilibrium potential, bulk concentration, concentration of oxidant, and those of reductants, respectively.

Electrochemical cells are classified into two types, a galvanic cell and an electrolytic cell. The former is that the electrochemical reaction occurs spontaneously, while the latter is in reverse. Typical galvanic cells are energy converting devices such as primary batteries and fuel cells. In the galvanic cell, the overpotential, difference in reduction potential between the thermodynamic and the measured value, has a negative effect on the total cell efficiency. The measured potential in the galvanic cell can be stated as the equation;

$$E = E^0 - \eta_{\text{cathode}} - \eta_{\text{anode}} - iR_s$$

where, η_{cathode}, η_{anode}, i, and R_s are overpotential of cathode and anode, current, solution resistance. To improve the cell efficiency, it is important to minimize the overpotential in the electrode where the electrochemical reaction takes place.

1.1.2. Proton Exchange Membrane Fuel Cell (PEMFC)

A fuel cell is an energy converting device, generating electricity from electrochemical reactions with an external feed of fuels. Like other galvanic cells such as batteries, fuel cells carried out the electrochemical reactions including oxidation and reduction in both part of electrodes the anode and cathode, respectively. Fuel cells are generally classified in accordance with using electrolytes; proton exchange membrane fuel cells (PEMFCs), alkaline fuel cells (AFCs), phosphoric acid fuel cells (PAFCs), molten carbonate fuel cells (MCFCs), and solid oxide fuel cells (SOFCs). (Table 1.1)

In particular to PEMFCs, it is intensively focused on the application of portable devices, automobiles residential power generators.[1-4] Typical fuels of the PEMFCs are hydrogen and oxygen gas in the anode and the cathode, respectively. For the anodic reaction, hydrogen molecules are converted to two proton with generation of two electrons at E = 0.000 V. Oxygen molecules with four electrons and proton are formed water molecule at E = 1.229 V at the cathode. (Figure 1.1) Owing to the thermodynamic relationship, a theoretical potential difference and efficiency are 1.229 V and 83 %, much higher than that of the combustion engine. The single cell, so-called the membrane electrode assembly (MEA), is mainly composed of membrane, catalyst/catalyst layer, gas diffusion layer (GDL), bipolar plates. (Figure 1.2) Membrane is an electrolyte to transport proton and water with a blocking layer between anode and cathode. The electrochemical reaction including hydrogen oxidation and oxygen reduction occurs in the catalyst/catalyst layer.

GDL is a flow channel for reactants and products. Bipolar plate acts as a support and current collector of the MEA. Among components of MEA the Nafion® based-membrane and the Pt based-catalyst/catalyst layer take a primary portion of the unit cost of electricity production. Especially in catalyst/catalyst layer, it is important to reduce the amount of Pt loading, that is, the kinetics of the electrochemical reaction is enhanced with respect to a unit Pt mass. In this line, U.S. department of energy supported ca. 33% of the funding to researches on the catalyst in 2010.[5] Therefore, many researches have been studied to improve the electrocatalytic activity of the Pt-based catalysts.

Table 1.1. Types of fuel cells with respect to using electrolyte.

	Electrolyte	Operating Temp. (°C)	Catalyst	Fuel
PEMFC	Polymer electrolyte	50~200	Pt	H_2
AFC	Alkaline solution	150~200	Pt	H_2
PAFC	Phosphoric acid	150~250	Pt	H_2
MCFC	Molten carbonate	600~650	Ni	H_2, CH_4
SOFC	Ceramic oxide	500~1100	Pervoskite	H_2, CH_4, CO

Anode : $2\ H_2 \rightarrow 4\ H^+ + 4\ e^-$	$E^0 = 0.000$ V
Cathode : $O_2 + 4\ H^+ + 4\ e^- \rightarrow 2\ H_2O$	$E^0 = 1.299$ V
Overall : $2\ H_2 + O_2 \rightarrow 2\ H_2O$	$\Delta E^0 = 1.299$ V

Figure 1.1. Electrochemical reactions in the PEMFC.

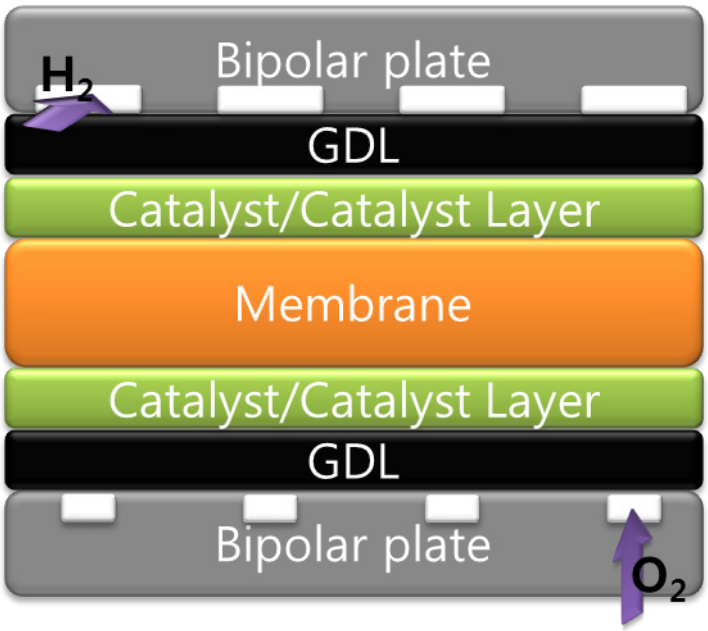

Figure 1.2. Schematic diagram of the MEA.

1.2. Electronic Structure and Oxygen Reduction

1.2.1. Electronic Structure for Catalysts

Reactions of catalysts are followed by the sequences listed below (Figure 1.3)[6]

1) Adsorption of the reactants on the surface of the solid.
2) Diffusion on the surface.
3) Breaking of some reactant bonds.
4) The creation of new ones to form the product molecules.
5) Desorption from the surface.

In particular to electrocatalysts, the electron transfer is involved in catalyzed processes including the ORRs. Retaining intrinsic electronic structures to make reactions possible toward adsorbate species, the d-band metals are used frequently as electrocatalysts. From the band theory, metals forms band structures, that is, the band like continuous energy states of electrons as a consequence that electronic orbital is overlapped each other. The frontier bands, taking the highest energy states, affect electron transfer reactions, i.e., electrocatalytic ones.

In case of d-band metal, the frontier s- and d-bands are influenced on the reaction pathway. When an adsorbate species is approached to d-band metals, it is known that s-bands widen their width due to the strong coupling with the

valance states of adsorbates which are broadened and stabilized by the interaction. The effect of interaction of s-bands is not totally different to the other metals; however, an interaction of d-band makes it possible that d-band metals attain catalytic activity unlike s-, p-band metals. The width of d-bands is narrow due to the small coupling matrix of d-orbital which is proportional to the band width.[7] If we consider simple one electron of atoms and molecules interacting with a metal surface, the valance states of adsorbate species divide electronic states into a bonding and an antibonding state because of the interaction with the d-bands, relatively narrow width. A bonding state has a lower energy level with respect to Fermi level of metals; on the other hand, an antibonding state shows resistive characters to adsorption on the metal surface with an unstable energy state.

The degree of split-off bonding and antibonding states is directly related to the tendency of chemisorptions. As shown in Figure 1.4, the strong chemisorptions lead, to the large extent, separation of two states in adsorbate species as well as the shift up of d-band center in metal species to the Fermi level due to decrease in width of d-band. Therefore, the d band center of metal is a descriptor which can show the strength of chemisorptions between a metal and an adsorbate.

For O_2, the valence 2p states interact with the s-bands (single resonance) and d-bands (a splitting of oxygen resonance into two) of transition metals. The coupling to the d states is essentially a two-level problem giving rise to a bonding and an antibonding state. From density functional theory (DFT) calculation[8], it is shown that the farther to the left and to the up side in the

periodic table result in the stronger bond formation. If the coupling to the metal s-states is approximately the same for each of the metals considered, the main trends in the chemisorption energies should be given by the coupling to the d-electrons. As we move to the left from copper, silver, or gold, the d-bands move up in energy, and increasingly more antibonding adsorbate-metal d-states become depopulated. The general trends are represented by the d-band center which is strongly coupled by the filling and the width of the d-bands. For a filled and deeper lying d-band, the oxygen 2p states have to become orthogonal to the metal d-states when they come into contact in accordance to Pauli repulsion which is proportional to the square of the adsorbate-metal d-coupling matrix element. For an unfilled d-band (the left of copper, silver, and gold), Pauli repulsion and the attractive interaction are affected due to the empty antibonding states.[6]

The trends of reactivity are determined by the energy of transition states which is equivalent to the kinetic barrier of reaction pathway. Nørskov and co-workers elucidated that the adsorption energy is linear relationship with the activation energy of reaction intermediates independent of reactant species,[9] so-called Brønsted–Evans–Polanyi lines.[10-11] They expected the high catalytic activity would be shown at binding energy between -1.4 ~ 0.8 eV, and solely depend on their adsorbate sites. Like the adsorption strength of adsorbate species, it can be characterized by the center of d-band. If the center of d-band goes up to the Fermi level, the reaction rate is increased in that the transition species is stabilized, i.e., kinetic barrier is lowered. However, moving to the left in the transition metal series gives a lower activation energy

but also stronger bonding of the reactants and thus less free surface area; “Sabatier principle”-type behavior.

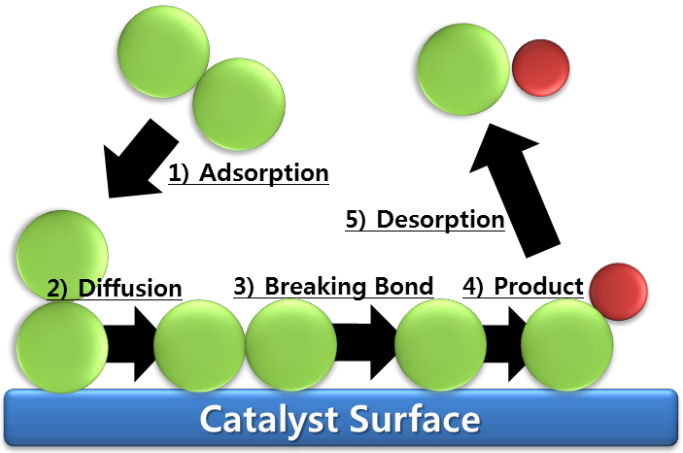

Figure 1.3. Reaction step on the catalyst surface.

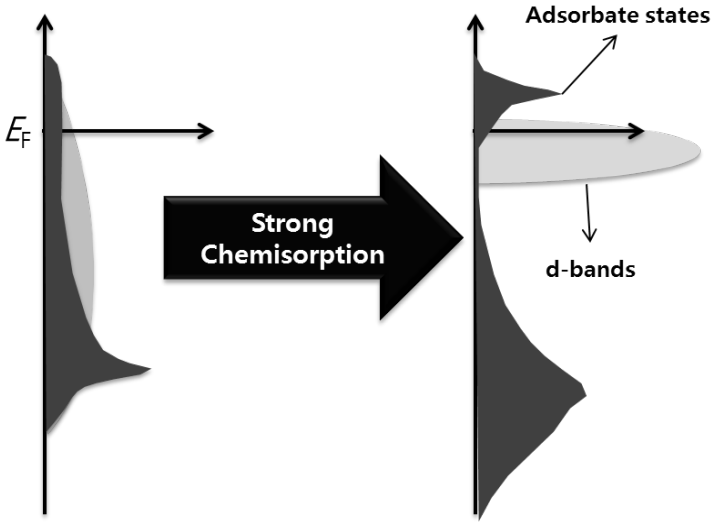

Figure 1.4. Density of states for adsorbate state interacted with the different coupling matrix.

1.2.2. Oxygen Reduction Reactions (ORRs)

In particular to oxygen reduction reactions (ORRs), platinum has the highest activity among the single metals, but is still room for improvement of its electrochemical reactivity.[12] The elementary steps of the ORR for Pt are proposed into the two mechanisms, the dissociative and the associative mechanism. (Figure 1.5) From the DFT calculations, the dissociative and the associative mechanism are dominant at a low and high current range, respectively. [4, 12-13]

The overpotential of ORRs for Pt is originated from too strongly adsorption of oxygen and hydroxyl group on the surface.[12, 14] Hence, in order to decrease overpotential of ORRs, it is favorable that the strength of chemisorbed species is slightly weakened, that is, the activation energy of reaction determined step (RDS) of ORRs goes to minimize value. To achieve this goal, we need to tailor the Pt electronic structure, the frontier d-band structure directly associated with the extent of chemisorption and the activation barrier. The electronic structure of Pt can be altered by changes in the surface structure with the different facets and the ligand effect including alloying.[15] The d-band structure of Pt is affected by the coordination number of the metal surface and varied with the exposed surface.[16] The ligand effect means the electronic structure of the targeted atom is tuned by the hybridization of electronic states with neighbouring atoms. One of the most common approaches is alloying with other metallic species. This effect also causes the shift of the frontier d-band structure of Pt by calculations [17-

18] and experimental results [19-21].

Adsorption of the spectator species is another problem to reduce the ORR kinetics in the acidic electrolyte, in which PEMFCs operate. During the electrochemical reactions, conjugated anions are specifically adsorbed on the metal surface, so-called, the specific anion adsorption. Particularly, the extent of specific anion adsorptions increases in the decreasing energy of solvation, that is, $F^- < ClO_4^- < SO_4^{2-} < Cl^- < Br^- < I^-$.[22] For that reason, the rate of the ORR in Pt is severely deactivated when to use electrolytes, the high degree of anion adsorption such as sulphuric, hydrochloric, and phosphoric acid. [23-25] Some studies have suggested to solve this problem by the ensemble (or third-body effect),[26] blockage of adsorption, the ligand effect[27-28], and modification of the surface structure.[29]

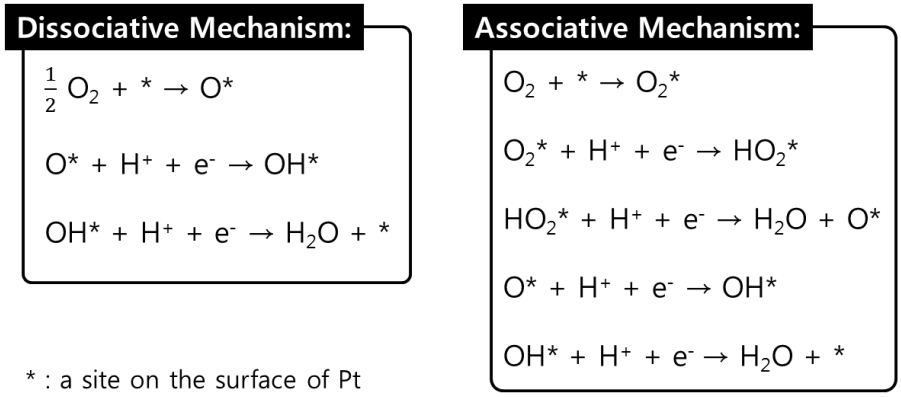

Figure 1.5. Two elementary steps of the ORR mechanism.

1.3. Preparation of Pt-Based Nano-Catalysts

1.3.1. Colloidal Reduction Method

Nanomaterials are attracted considerable attention for the electrochemistry field due to their unique properties. The U.S. National Nanotechnology Initiative (NNI) refers that "Nanotechnology is the understanding and control of matter at the nanoscale, at dimensions between approximately 1 and 100 nanometers, where unique phenomena enable novel applications." Nanomaterials can be obtained by two approaches such as a "top-down" and a "bottom-up" approach. (Figure 1.6) A top-down approach is that a nano-sized material is acquired from a bulk one generally utilizing physical equipment including physical vapor deposition, ball milling, and electrodeposition. The colloidal reduction method is one of the frequently used systems as a bottom-up approach to synthesize nanomaterial. The colloidal reduction preparation of nanoparticles was generally fulfilled by a chemical route with some chemicals, which consist of precursors, solvents, reducing agents, and capping agents. According to the previous studies [30-33], both nucleation and growth steps are controlled at the stage of forming nanomaterials, *i.e.*, the nuclei formed from the precursor should be grown slowly. If the growth rates cannot be controlled, the dissolved particles will diffuse toward larger particles and deposit to minimize the surface free energy through a process known as Ostwald ripening. Once Ostwald ripening occurs, the particle size distribution increases. To prevent this aggregation of nanomaterials, the surface capped

species or the capping agent is primarily important to synthesize the nano-sized particles. The capping agents can be stabilized on the surface of the nanoparticles by lowering the rate of growth through either steric or electrostatic stabilization. Adsorbed to the specific species and facets of nanomaterials, the capping molecules can be mixed for the specific purpose including controls of the surface composition and shape.

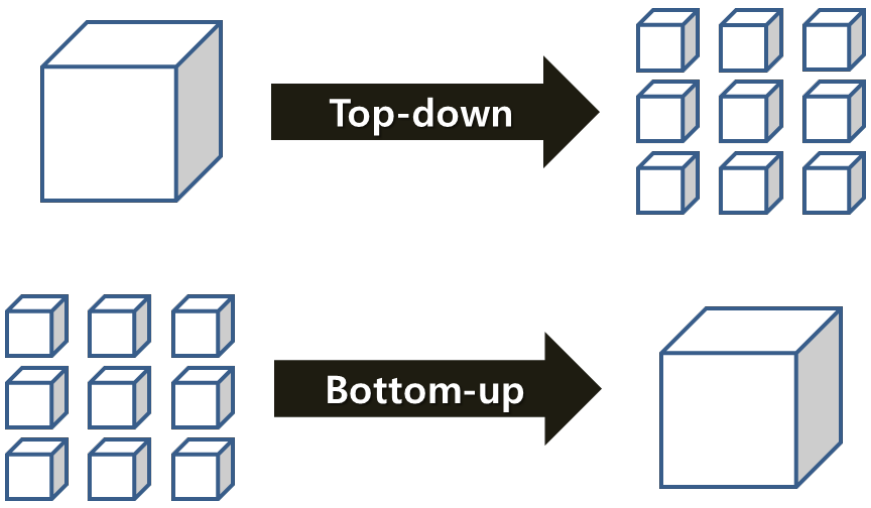

Figure 1.6. Two approaches for preparation of nanomaterials.

1.3.2. Preparation of Pt-Based Nanoparticles

When Pt-based nanoparticles are prepared via the colloidal reduction method, chemicals, participated in the reaction, are significantly affected to the physical and chemical properties. Particularly, the surface composition and morphology are determined by interactions between the capping agent and the metallic species. Among capping molecules, the oleylamine ($CH_3(CH_2)_7CH=CH(CH_2)_7CH_2NH_2$) and the oleic acid ($CH_3(CH_2)_7CH=CH(CH_2)_7COOH$) are most widely used for the preparation Pt-based nanoparticles, especially in case of Pt-3d metal nanoparticles. Due to the Lewis acidity, oleylamine (soft Lewis acid) is strongly adsorbed on the surface of Pt (soft Lewis base) resulting in stabilization of surface energy. This avid interaction regards as an undesirable phenomenon due to blocking the active sites when to apply nanoparticles to catalyst. Therefore, the surface cleaning process should be performed to discard the adsorbed species.[34-53] (Table 1.2) The heat treatment is a common process to alter the electrochemical properties of the synthesized nanoparticles. It is believed that the heating process induces a profitable effect to the Pt-based nanoparticles. However, it is still elusive how to affect the electronic structure, which is related with catalytic activities.

Table 1.2. Surface cleaning process for capping agent.

Materials	Methods for removals	Ref.
Pt-Mn	Heat (600 ℃, 30 min) + UV-ozone treatment	[49]
Pt-Co/C	Heat (250 ℃, 3 h, Ar)	[50]
Au/$FePt_3$	Heat (450 ℃, 12 h, Air)	[51]
Pt-Ru	Acid (80 ℃, 12 h)	[52]
Pd	Acid (80 ℃, 12 h)	[53]

1.4. Aim of this Thesis

The sluggish kinetics of the ORR is one of most significant problems to commercial application of the PEMFC. As discussed previous sections, the electrocatalytic activity for the ORR can be enhanced by tuning the frontier d-band structure of Pt species. Due to the high surface area, Pt-based nanoparticles are inevitably attracted as an oxygen reduction electrocatalyst. Although the colloidal reduction method is a facile process to produce Pt-based nanoparticles, the understandings of the prepared environments such as the capping molecules and the heat treatments, significantly affected to the electronic structure of Pt-based nanoparticles are needed to design an advanced electrocatalysts.

The aim of this thesis is primarily on the relationship between the electrochemistry in the ORR and the electronic structure of Pt-based nanoparticles. (Figure 1.7) To achieve this goal, three subjects, concerned in the general consideration to the Pt-based nanoparticles, are investigated, including the preparation stage, as-prepared state and the post-treatment process. (Figure 1.8) Relationship of these effects can deepen our understandings of electrochemistry in the ORR, and posit how to engineer the nano-sized electrocatalysts.

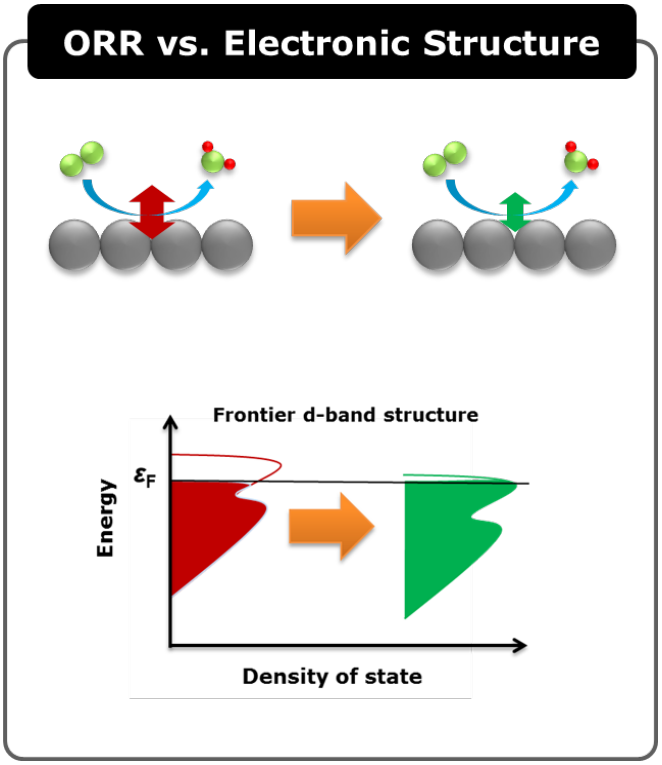

Figure 1.7. Schematic diagram of the electrochemistry in the oxygen reduction and electronic structure.

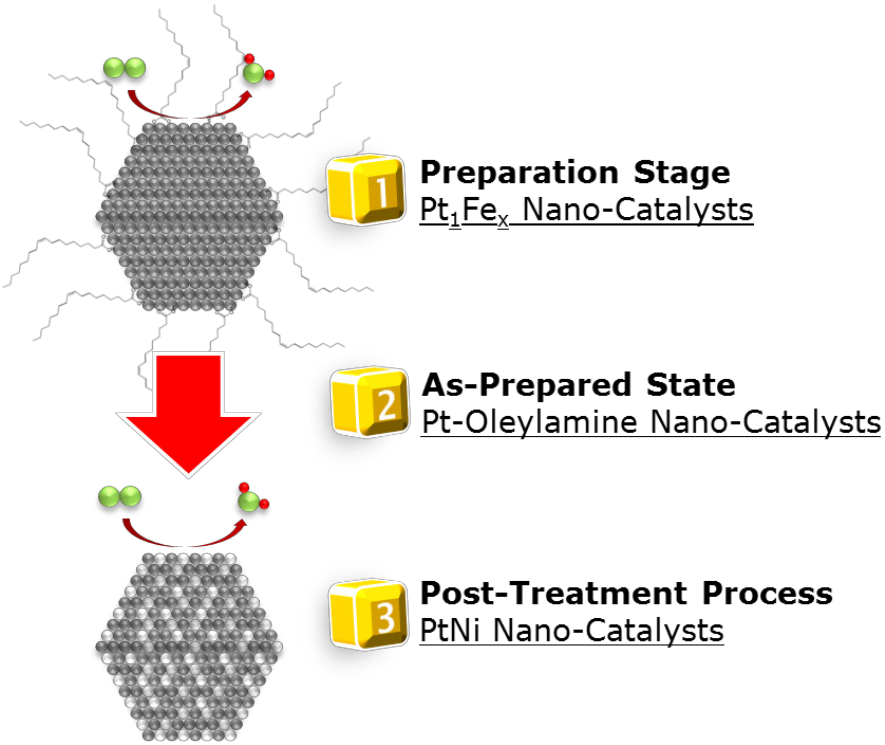

Figure 1.8. Subjects of this thesis.

Chapter 2. Experimental

2.1. Preparation Stage: Pt_1Fe_x(x=1, 2, 3) Nanoparticles

2.1.1. Chemicals and Materials

Platinum(IV) chloride ($PtCl_4$, 99.99+%), iron(II) chloride tetrahydrate ($FeCl_2$ $4H_2O$, 99.99+%) oleic acid (90%), sodium borohydride ($NaBH_4$, 99.99%), and Nafion perfluorinated resin solution (Nafion, 5 wt% in lower aliphatic alcohols and water) were purchased from Aldrich. Anhydrous ethanol (EtOH, 200 proof, 99.5+%) was received from Sigma-Aldrich. 2-propanol (CHROMASOLV) was purchased from Fluka. Carbon black (Vulcan XC-72) and carbon supported platinum (Pt, HiSpec 3000, 20wt%) were received from Carbot corporation and Alfa Aesar respectively.

2.1.2. Preparation of Nano-Catalysts

Pt_1Fe_x bimetallic nanoparticles with the Fe-rich surface were simply prepared via wet chemical reactions using anhydrous ethanol. A typical procedure is as follow; carbon black (1500 mg), oleic acid (0.071 mL) and EtOH (200 mL) were loaded in beaker and sonicated. Then adequate amounts of $PtCl_4$ and $FeCl_2$ $4H_2O$, the molar ratio of Pt:Fe = 1:1, 1:2, and 1:3, were added into the solution with vigorously stirring. The final amount of metal loading was set as 20 wt%. After 2 h, a reducing agent, $NaBH_4$ (1500 mg),

was immediately introduced into the above solution and stirred overnight for the complete reaction. The resultant products were isolated by filtration and washed ethanol and deionized water. Finally, three bimetallic nanoparticles were dried in a vacuum and collected. Based on their nominal Pt to Fe ratio, these nanoparticles with the Fe-rich surface were denoted as Pt1Fe1_RS, Pt1Fe2_RS, and Pt1Fe3_RS, respectively. To develop the Pt-Fe mixed surface, the heat treatment was carried out for each sample in a reducing atmosphere, H_2 (5%)/Ar (95%) at 300 ^oC for 1 hour and subsequently cooled down in Ar (99.999%) into the room temperature. Also, the nanoparticles with the Pt-Fe mixed surface were referred as Pt1Fe1_MS, Pt1Fe2_MS, and Pt1Fe3_MS, respectively.

2.1.3. Characterization

Transmission electron microscope (TEM, JEOL JEM-2010) was operated at an acceleration voltage of 200 kV. High resolution-TEM (HR-TEM) images were obtained using Tecnai F20. (200 kV, FEI) High resolution powder diffraction (HRPD) spectra were measured in a 9B beam line of Pohang Light Source-II (PLS-II, 3GeV). The incident beam was the wavelength of 1.5490 Å and a step scan was carried out from 15° in 2θ with 0.02° increments and 0.5° overlaps to the next detector bank up to 135.5° in 2θ. Each sample was rotated during the measurement to discard preferred orientation. The X-ray absorption near-edge structure (XANES) of Pt L_3 edge (E_0= 11,564eV) was measured using an 8C beam line of PLS-II. The incident beam was detuned

by 30% to remove higher harmonics. All spectra were recorded by transmission mode after taking place energy calibration using Pt foil as a reference. Absorption intensity was normalized by ATHENA software of IFEFFIT programs. Inductively coupled plasma-atomic emission spectra (ICP-AES, Shumdzu, JP/ICPS-7500) analysis.

A catalyst ink was produced mixing 15 mg of the electrocatalysts, 0.03mL of deionized water, 1.2 mL of 2-propanol, and 0.0858 mL of Nafion solution. After mixing thoroughly, 0.007 mL ink was pipetted onto the glassy carbon working electrode (5mm-diameter, 0.196 cm^{-2}). The electrochemical measurement was carried out using a three electrode system; a electrocatalysts coated glassy carbon working electrode, a platinum wire counter electrode, and an Hg/Hg_2Cl_2 reference electrode (3.5 M KCl) containing 0.1 M $HClO_4$. All electrochemical experiments were performed using AUTOLAB potentiostat (Eco Chemie, PGSTAT101) and reported against the reversible hydrogen electrode (RHE). Before obtaining electrochemical data, the pretreatment (cyclic voltammetry at a scan rate = 50 mV s^{-1}) was conducted for 100 cycles between 0.05 and 1.05 V in a solution saturated with Ar (99.999%) to obtain a stable voltamogram. Subsequently, cyclic voltamograms (CVs) were measured at a scan rate, 20 mVs^{-1}. For measuring CO stripping curves, high purity CO gas (99.99+%) was introduced into the solution with applying a constant potential (0.05 V) and displacement current was recorded until reaching to zero, *i.e.* adsorption of CO molecules onto electrocatalyst was completed. After removing bulk CO in electrolyte with a flow of Ar, CVs of CO oxidation curves were obtained at a scan rate, 20 mV s^{-}

[1]. All measurements were conducted at 20 ^{o}C in each experiment. Polarization curves for the ORRs were recorded using rotating disk electrode (RDE) at a rotating speed, 1600 rpm, with a scan rate, 5 mV s^{-1}, in a solution saturated with O_2 (99.995%). A commercial Pt/C (20wt%, Johnson-Matthey Co.) was used as a reference electrocatalyst and denoted as Pt. The kinetic current density was obtained by following equation;

$$\frac{1}{j} = \frac{1}{j_{l,c}} + \frac{1}{j_k}$$

where j, $j_{l,c}$, and j_k are measured, cathodic limiting, and kinetic current density, respectively. To compare the extent of enhancement in ORR kinetics, we used a term, improvement factor, which is the ratio of specific kinetic current densities versus Pt at 0.9 V.

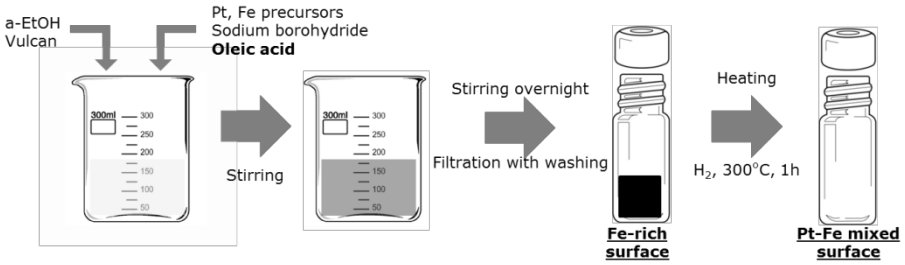

Figure 2.1. Preparation procedures of Pt_1Fe_x (x = 1, 2, 3) nanoparticles.

2.2. As-Prepared State: Pt-Oleylamine Nanoparticles

2.2.1. Chemicals and Materials

Pt/C (HiSPEC^{TM} 9000, 60 wt%), ethanol (> 99.9%), and oleylamine ($C_{18}H_{37}N$) was purchased from Johnson Mattey Co., Samchun chemical, and TCI. Nafion perfluorinated resin solution (Nafion, 5 wt% in lower aliphatic alcohols and water) were purchased from Aldrich. 2-propanol was purchased from Junsei.

2.2.2. Preparation of Nano-Catalysts

In order to compare the carbon-supported platinum electrocatalysts (Pt), oleylamine modified Pt/C (Pt _OA) were prepared by simply mixing Pt/C and oleylamine in an organic solvent. All chemicals were purchased and treated without purification. The detail procedure is as follows; 0.1 g of Pt/C Johnson was dissolved in 100 mL of ethanol. After 10 min sonication, 30.8, 92.4, and 154.0 μmol of oleylamine, which is 10, 30, and 50 mol % of platinum based on the nominal ratio, was added to the solution with vigorous stirring and referred as Pt_OA01, Pt_OA03, and Pt_OA05, respectively. After additional stirring overnight, the solution was filtered and the obtained particle was dried in a vacuum at room temperature.

2.2.3. Characterization

HR-TEM images were obtained a JEOL-2010 at an acceleration voltage of 200 kV using a carbon coated cooper grid. Elemental analysis was carried out using a US/CHNS-932 (LECO Corp.). To conduct the electrochemical measurements, a catalyst ink was produced by mixing 0.015 g of the electrocatalysts, 30 μL of deionized water, 1200 μL of 2-propanol (Junsei), and 85.8 μL of a Nafion solution (Aldrich, 5 wt.%). After mixing and sonication, the ink was dropped onto glassy carbon as the working electrode by a micropipette and dried in an oven. The working electrode was transferred to a three electrode system, which consisted of a saturated calomel electrode (SCE) as the reference electrode, and Pt wire as the counter electrode in various electrolytes; 0.1 M $HClO_4$ (Sigma-Aldrich, 70 %), 0.1 M $HClO_4$ + 0.1 M H_3PO_4 (Sigma-Aldrich, 85 %). All electrochemical measurements were carried out using an AUTOLAB potentiostat (Eco Chemie, PGSTAT) at 20 ^oC and the potentials were standardized with respect to a reversible hydrogen electrode (RHE). Before all measurements, pre-cycling step was performed until obtaining a stable voltamograms in a solution saturate with Ar. Cyclic voltammetry (CV) was conducted at a 20 mV s^{-1}. The electrochemical surface active area (ESA) was calculated based on the potential range in which platinum adsorbs underpotentially deposited hydrogen (H_{upd}) and the specific charge of platinum, 0.21 mC $cm^{-2}{}_{Pt}$. Also, the surface coverage was obtained by the ratio of the ESA for Pt_OA relative to that for Pt.

Rotation disc electrode (RDE) was used for measurement of oxygen reduction reactions (ORRs) at a scan rate of 5 mV s^{-1} and a rotating speed of 1600 rpm. The kinetic current density was calculated by the following

equation:

$$\frac{1}{j} = \frac{1}{j_{l,c}} + \frac{1}{j_k}$$

where j, $j_{l,c}$, and j_k are measured, cathodic limiting, and kinetic current density, respectively.

Synchrotron-based photoelectron spectroscopy (PES) was performed at 8A1 beamline connected to U7 undulator in Pohang accelerator laboratory (PAL, 3 GeV). All spectra were measured at 630 eV and calibrated by a binding energy of Au $4f_{7/2}$, 84 eV. To calculate the d-band center (ε_d), we carried out integration of valence band structure (~ 10 eV vs. Fermi level) using XPSPEAK 4.1 software as following equation;

$$\varepsilon_d = \frac{\int N(\varepsilon)\,\varepsilon\, d\varepsilon}{\int N(\varepsilon) d\varepsilon}$$

where N(ε) is the density of states or intensity of photoelectron spectra after Shirely background correction.

X-ray absorption spectroscopy (XAS) was measured at 7D beamline in PAL. Pt L_3 edge, transition $2p_{3/2}$ to $5d_{5/2}$ by dipole selection rule, was detected at E_0 = 11564 e. The incident beam was monochromatized by two set of Si(111) crystals and detuned 30 % for minimization of higher order harmonics. The absorption energy was calibrated Pt foil before measurements. The X-ray absorption near-edge spectroscopy (XANES) and extended X-ray absorption fine structure spectroscopy (EXAFS) were analyzed using ATHENA and ARITEMIS software of IFEFFIT programs.

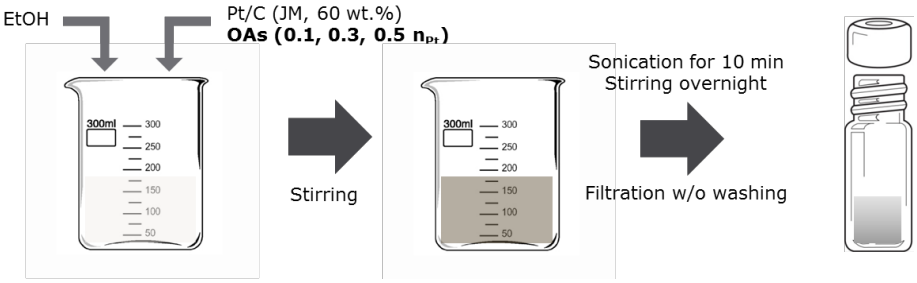

Figure 2.2. Preparation procedures of Pt-OA nano-catalysts.

2.3. Post-Treatment: Pt_1Ni_1 and Pt_2Ni_1 Nanoparticles

2.3.1. Chemicals and Materials

Chemicals were purchased from Sigma-Aldrich; Platinum chloride ($PtCl_4$, 99.99+%), nickel chloride hexahydrate ($NiCl_2$ $6H_2O$, 99.999%), oleic acid ($CH_3(CH_2)_7CH=CH(CH_2)_7COOH$, 90%), sodium borohydride ($NaBH_4$, 99.99%),anhydrous ethanol (CH_3CH_2OH, 99.5+%), Nafion perfluorinated resin solution (Nafion, 5 wt% in lower aliphatic alcohol and water), bismuth(III) oxide (Bi_2O_3, 99.999%)and methanol (CH_3OH, 99.9>%). Carbon black (Vulcan XC-72) and carbon supported platinum (Pt, HiSpec 3000, 20 wt%) were received from Carbot corporation and Alfa Aesar, respectively.

2.3.2. Preparation of Nano-Catalysts

Carbon supported PtNi nanoparticles were prepared via the one-pot colloidal reduction method. A brief procedure is summarized as follow; 0.071 mL of oleic acid was added in 200 mL of anhydrous ethanol and sonicated. Subsequently, 0.0504 g of $PtCl_4$ and 0.0357 g of $NiCl_2$ $6H_2O$ were mixed with a vigorous stirring in the carbon dispersed solution. After stirring for 2 hours, 0.1500 g of $NaBH_4$ was immediately added into the solution to reduce metal ions and stirred overnight. The solution was filtered with ethanol and dried in a vacuum. All process was conducted under the room temperature and ambient atmosphere. The obtained powder was annealed in a flow of H_2/Ar (5/95 vol%)for 1 hour at the different

temperature, 300 and 700 ^{o}C, denoted as PtNi/C_300 and PtNi/C_700, respectively.

Carbon supported Pt_2Ni_1 bimetallic nanoparticles were synthesized by the similar procedure. A synthetic route was briefly summarized below; 0.15 g of carbon black and 71 μL of oleic acid were mixed in anhydrous ethanol. After sonication for 30 min, the mixturevigorously stirred with the addition of $PtCl_4$ and $NiCl_2$ $6H_2O$ for 2 h and 0.15 g of $NaBH_4$ was introduced. The colloid were filtered and washed with ethanol. Then, the powder was dried and collected. (PtNi_AP)The total metal loading of nanoparticles was 40 wt%. Lastly, we performed heat treatments with the different atmosphere, i.e. argon (Ar, 99.999%), hydrogen (H2, H_2(5%)/Ar (95%)), and compressed air (Air), at 300 ^{o}C for 1h. These nanoparticles were denoted as PtNi_Ar, PtNi_H2, and PtNi_Air, respectively.

2.3.3. Characterization

For Pt_1Ni_1 nanoparticles, high resolution-transmission electron microscope (HR-TEM) was measured using Titan 80-300 (300 kV, FEI) and Tecnai F20 (200 kV, FEI). Cs-corrected scanning transmission electron microscope (STEM) was obtained by JEM-ARM200F (200 kV, JEOL)equipped with energy dispersed spectrometer (EDS, BrukerQuantax 400). High resolution powder diffraction (HRPD) was carried out in 9B beamline of Pohang Light Source-II (PLS-II, 3 GeV). The incident beam was a wavelength of 1.5490 Å using a double-crystal Si(111) monochromater. A scan range of 2$\theta$was

$15^{o}< 2\theta <135^{o}$ with 0.02^{o} increments and 0.5^{o} overlaps to the next detector. X-ray absorption fine structure (XAFS) measurements were performed in 8C beam line of PLS-II. The Pt L_3 edge, transition from Pt $2p_{3/2}$ to $5d_{5/2}$, was detected at E_0 = 11,564 eV and calibrated by Pt foil. The analysis of Pt L_3 absorption edge was carried out using ATHENA and ARITEMIS software of IFEFFIT programs. X-ray photoelectron spectroscopy (XPS) was measured using Thermo Sigma Probe with Al K_α radiation. All spectra were calibrated with the C-C peak of C 1s orbitals as 284.6 eV. The peaks were fitted by XPSPEAK 4.1 software package. To analyse quantitative information, inductively coupled plasma-atomic emission spectroscopy (ICP-AES, Sumdzu, JP/ICPS-7500) and elemental analysis (EA, LECO corp. US/CHNS-932) were conducted.

For Pt_2Ni_1 nanoparticles, X-ray diffraction (XRD, Rigaku D/MAX 2500) spectra were obtained with Cu K_α(0.1541 nm) at 40 kV and 200 mA. The scan range was $20^{o}< 2\theta < 80^{o}$ at 2^{o} min^{-1}. Transmission electron microscope (TEM, JEOL JEM-2010) was operated at an acceleration voltage of 200 kV. X-ray absorption near edge structure (XANES) measurement was carried out in an 8C beam line of Pohang Light Source-II (PLS-II, 3 GeV). All measurements were calibrated with a reference Pt or Ni foil and detected transmission mode. The spectra was normalized by ATHENA software of IFEFFIT package. X-ray photoelectron spectroscopy (XPS, Thermo Sigma Probe) experiments were conducted by Al K_α as an X-ray source. All spectra were calibrated by C 1s as 284.6 eV. The obtained peaks were deconvolutedby XPSPEAK 4.1 software.To acquire quantitative

information, we carried out inductively coupled plasma-atomic emission spectra (ICP-AES, Shumdzu JP/ICPS-7500) analysis and elemental analysis (EA, LECO corp. US/CHNS-932) of C, H, N.

The three electrode cell was used to characterize the electrochemical measurement of carbon supported PtNi nanoparticles; working (catalyst ink on a glassy carbon electrode), reference (saturated calomel electrode, SCE), and counter electrode (Pt wire). All measurements were performed using an AUTOLAB potentiostat (Eco Chemie, PGSTAT) at 20 ^{o}C. Potentials were referred as a reversible hydrogen electrode (RHE) to calibrate pH-dependency. To compare Pt nanoparticles, a commercial carbon supported Pt, denoted as Pt/C, was used as a reference. A catalyst ink composed of 0.015 g of the catalyst, 1200 μL of methanol, and 85.8 μL of Nafion solution. Catalyst ink was transferred to glassy carbon electrode after sonication to obtain homogeneous solution. To confirm electrochemical stability, pre-potential cycling was carried out at a potential between 0.05 and 1.05 V for 100 cycles with a scan rate, 50 mV s^{-1}, in 0.1 M $HClO_4$ and a saturated Ar (99.999%). CO stripping measurement was performed after the completion of adsorption of CO at 0.5 V with a high purity CO gas (99.99+%). Cyclic voltamograms (CV) of CO oxidation curves was acquired in 0.1M $HClO_4$with a scan rate, 20 mV s^{-1}, after removal of residual CO gas into Ar. Irreversible adsorption of Bi was carried out by immersing the electrode to 10^{-4} M Bi_2O_3 solution in 0.1 M $HClO_4$. The electrode was washed with deionized water and put into the electrochemical cells. The CVs were obtained from the modified electrocatalysts. The

experimental details were described in Supporting Information. Polarization curves for the oxygen reduction reaction (ORR) were conducted using rotating disc electrode (RDE) in 0.1M $HClO_4$ with a saturated O_2 (99.995%) at a scan rate and rotating speed, 5 mV s^{-1} and 1600 rpm, respectively. The kinetic current density of the ORR was calculated by the equation;

$$\frac{1}{j} = \frac{1}{j_{l,c}} + \frac{1}{j_k}$$

where, j, j_{lc}, and j_k are measured, cathodic limiting, and kinetic current density, respectively. Polarization curves were corrected by the blank CV, measured with the same condition of the ORR except for Ar-saturated atmosphere. Specific or mass activity (vs. Pt/C) were defined as the extent of enhancement of the specific or mass kinetic current density (j_k) toward Pt/C at 0.9 V, i.e., $j_{k,PtNi/C}$ / $j_{k,Pt/C}$.

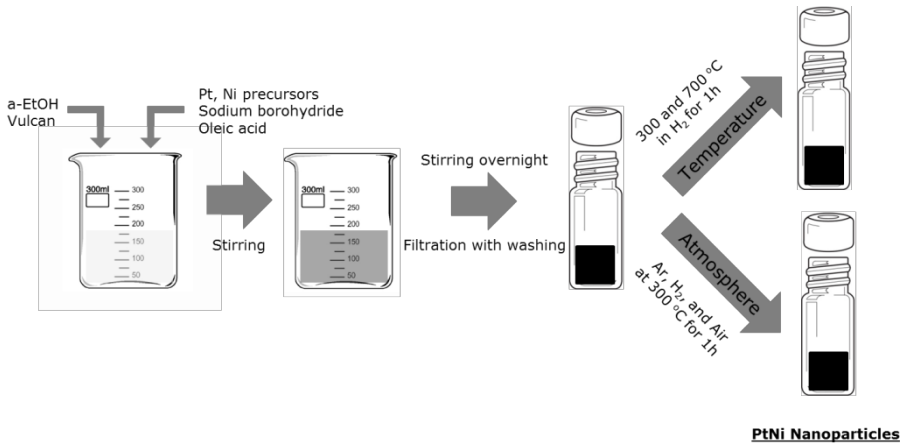

Figure 2.3. Preparation procedures of PtNi nano-catalysts with the thermal annealing.

Chapter 3. Results and Discussion

3.1. Preparation Stage: Pt_1Fe_x(x=1, 2, 3) Nanoparticles

3.1.1. Synthesis and Morphology

Carbon supported PtFe bimetallic nanoparticles with the Fe-rich surface were prepared using a single capping molecule, oleic acid. The oleic acid, one of the most commonly used capping agents, affect their composition and size during synthesis of Pt-3d metal bimetallic nanoparticles.[43] In particular, being a soft Lewis acid, platinum cannot be stabilized by oleic acid, a hard Lewis base, when to form PtFe nanoparticles.[49] On the other hand, the oleic acid was adsorbed on the surface of iron nanoparticles by strong interaction with –OOC functional group. [45, 54] These results were also correlated with the fact that oleic acid used alone in the preparation of Pt-rich PtFe nanoparticles, Pt_3Fe, resulted in precipitate and no re-dispersion in the hexane.[41] Because the difference of the standard reduction potential between the Pt ($PtCl_4^{2-}/Pt^0$, E^o = 0.73V) and Fe (Fe^{2+}/Fe^0, E^o = - 0.447V) is quite large enough, the nucleation of the Pt occurs in the early stage of the reduction and Fe nuclei is subsequently deposited on the Pt nanoparticles in the presence of the strong reducing agent, the borohydride ($B(OH)_3/BH_4^-$, E^o = - 0.481V).[44] In this reason, previous literatures have often reported that PtFe nanoparticles developed a Pt-rich core and Fe-rich shell.[45, 48, 54] Once PtFe bimetallic species are

prepared via borohydride reduction at ambient conditions, it can be expected that the Fe-rich surface was easily stabilized by the capping agent, oleic acid. (Figure. 3.1) As shown in Figure 3.2, the well-dispersed carbon supported PtFe nanoparticles (20 wt% loading) was examined by transmission electron microscope (TEM) images. Interestingly, there are different aspects of the reduced fast Fourier transform (FFT) spectra obtained from the high resolution-TEM (HR-TEM) about each nanoparticle. For the Pt_1Fe_1 nanoparticle with the Fe-rich surface, *i.e.*, Pt1Fe1_RS, the d-spacing value, calculated by the additional diffuse spot (red circles in Fig. 1(a)), was *ca*. 0.20 nm corresponding with that to Fe(111).[55] This result suggested that the separation of Pt and Fe species take place under the synthetic environment. It is also demonstrated that the PtFe nanoparticles with the Fe-rich surface were successfully prepared in both high loading (40 wt% loading) and absence of carbon supports. (Figure 3.4(a) and (b)) However, the bimetallic PtFe nanoparticles agglomerated when Pt to Fe ratio was > 1, *i.e.*, the Pt-rich condition. (Figure 3.4(c)) This result would carefully interpret that the Fe contents is a crucial factor to prepare PtFe nanoparticle in this reaction system due to avid interaction between Fe and –OOC group in the oleic acid. From ICP-AES measurement, the compositions of Pt1Fe1_RS, Pt1Fe2_RS, and Pt1Fe3_RS were $Pt_1Fe_{1.0}$, $Pt_1Fe_{2.2}$, and $Pt_1Fe_{3.1}$, respectively, which remain nearly identical without the significant loss, relative to the initial Pt/Fe proportion of precursors. (Table 3.1) To confirm the preferential interaction of the capping agent, oleic acid, we prepared carbon supported Pt-M (M = Co, Ni, Cu, and Au)

bimetallic nanoparticles with the same reaction system. Figure 3.5 showed the electron microscope images of Pt_1Co_1, Pt_1Ni_1, Pt_1Cu_1 and Pt_1Au_1 nanoparticles. In case of 3d metal including Co, Ni, and Cu, the standard reduction potentials are far lower than Pt and the Lewis acidity is gradually increased in the periodical order, Co > Ni > Cu. According to TEM images, the dispersity of nanoparticles were getting poorer as increase in Lewis acidity, *i.e.*, oleic acid cannot be stabilized on the surface of bimetallic nanoparticles. Considering the Au is higher reduction potential as well as Lewis acidity than Pt, the carbon supported Pt_1Au_1 nanoparticles exhibited the most inferior morphology among the bimetallic nanoparticles. Therefore, we can conjecture two determinants to form the small sized nanoparticles, the standard reduction potential and the Lewis acidity; affects the syntheses of Pt-based bimetallic nanoparticles within the framework of the proposed reaction system, preferential interaction of the capping agent. To develop the Pt-Fe mixed phase on the surface of nanoparticles (PtFe_MS), we carried out that the nanoparticles with the Fe-rich surface, (PtFe_RS) were annealed in the flow of reductive atmosphere, H_2/Ar (5/95 vol%) at 300 ^oC for 1 hour. In the light of difference in the surface segregation energies between Pt and Fe,[56-57] it can be expected that Pt atoms would diffuse out onto the surface of nanoparticles, simultaneously with conversion the Fe-rich phase to the PtFe mixed one. (Figure 3.1) The compositions of Pt1Fe1_MS, Pt1Fe2_MS, and Pt1Fe3_MS were $Pt_1Fe_{1.0}$, $Pt_1Fe_{2.3}$, and $Pt_1Fe_{3.3}$, respectively, similar to the PtFe_RS. (Table 3.1) As shown in the particle size distribution (Figure 3.5) calculated from the low magnification

TEM images (Fig. 3.2 and 3.3), the average particle sizes of nanoparticles with the Fe-rich surface were *ca*. 2.0, 1.9, and 1.7 nm for Pt1Fe1_RS, Pt1Fe2_RS, and Pt1Fe3_RS, respectively. In case of the Pt-Fe mixed surface, the average particle sizes were slightly increased after the heat treatment process, that is, *ca*. 2.2, 2.2, and 2.1 nm, respectively.

Table 3.1. Fe/Pt ratio by ICP-AES measurement.

Fe/Pt ratio	Pt_1Fe_1	Pt_1Fe_2	Pt_1Fe_3
Fe-rich surface (PtFe_RS)	1.0	2.2	3.1
Mixed Pt-Fe Surface (PtFe_MS)	1.0	2.3	3.3
PtFe_MS after the electrochemical reaction	0.6	1.5	0.8

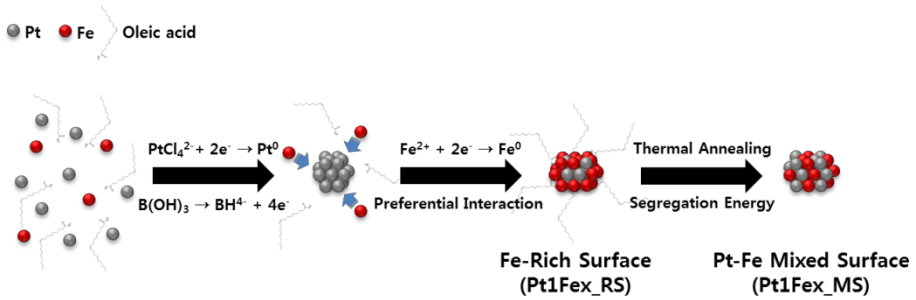

Figure 3.1. Schematic diagram of the Pt-Fe nanoparticles with the Fe-rich surface (PtFe_RS) and the Pt-Fe mixed surface (PtFe_MS).

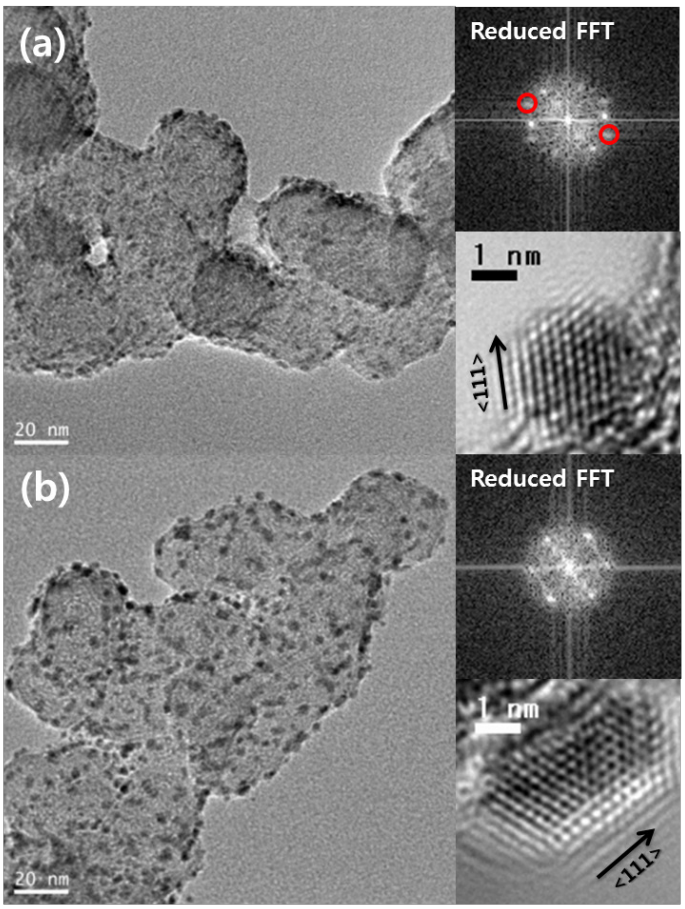

Figure 3.2. TEM images of Pt_1Fe_1 nanoparticles with (a) Fe-rich (Pt1Fe1_RS) and (b) the Pt-Fe mixed surface (Pt1Fe1_MS). (Left) HR-TEM images and their reduced fast Fourier transform (FFT) spectra. (Right)

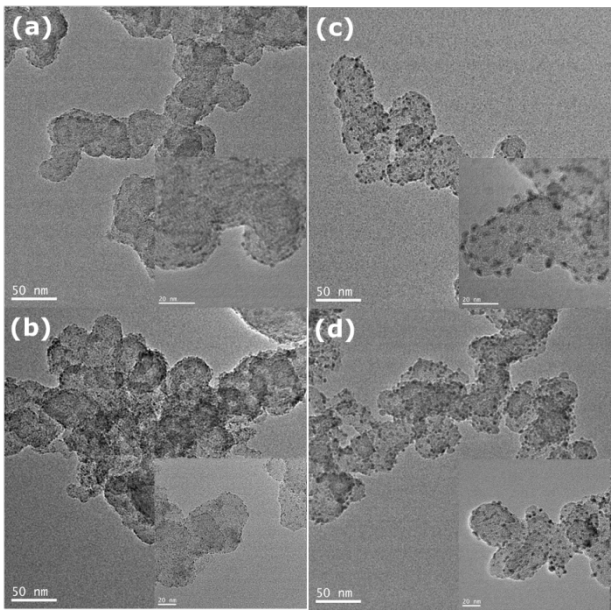

Figure 3.3. TEM images of (a) Pt_1Fe_2_RS, (b) Pt_1Fe_3_RS, and (c) Pt_1Fe_2_MS, (d) Pt_1Fe_3 _MS nanoparticles.

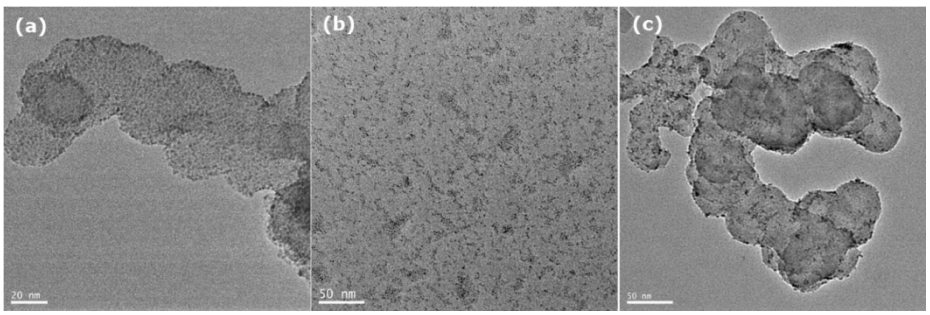

Figure 3.4. TEM images of (a) Pt_1Fe_1(40wt%)/C, (b) Pt_1Fe_1 without support, and (c) Pt_2Fe_1(20wt%)/C.

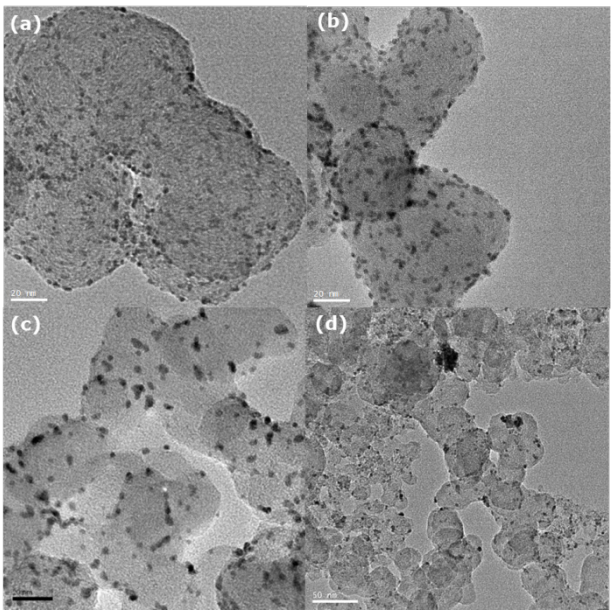

Figure 3.5. TEM images of (a) Pt_1Co_1, (b) Pt_1Ni_1, (c) Pt_1Cu_1, and (d) Pt_1Au_1(20 wt%)/C.

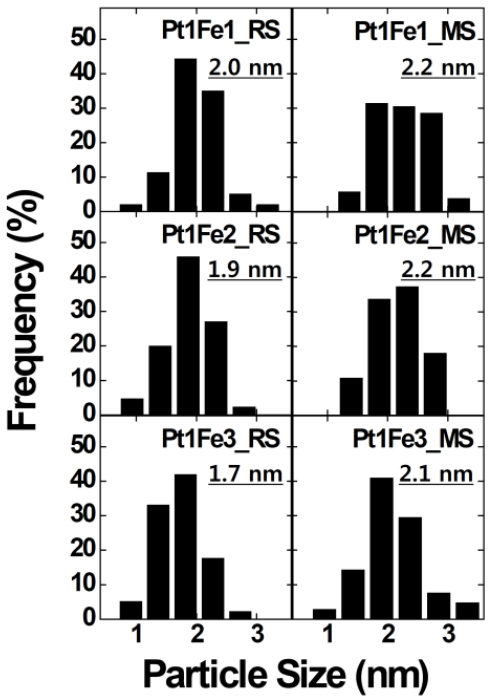

Figure 3.6. Particle size distribution and the average size of PtFe_RS (Left) and PtFe_MS (Right).

3.1.2. Structural Characterization

The bulk crystallographic structure of nanoparticles was examined by the synchrotron based HRPD patterns. (Figure 3.7(a)) For the PtFe_RS, the nanoparticles cannot form well-ordered crystal structure. As discussed earlier, it is likely that Pt and Fe phase were separated due to the preparation conditions, *i.e.*, the preferential interaction of Fe-OOC. Broad peaks were detected throughout the scan range including the broad peak at 2θ = *ca.* 25° associated with the carbon support. After the formation of the Pt-Fe mixed phase, however, XRD peaks of PtFe nanoparticles clearly indicated the Pt_1Fe_1 face-centered cubic (*fcc*) structure at 2θ = *ca.* 41, 47, and 68° assigned as (111), (200), and (220), respectively.[58] This structural change might be derived from diffusing out Pt located in the core part of the nanoparticle, resulting in formation of *fcc* structure by the difference in the segregation energies between Pt and Fe.[25,26] The peaks related with the fcc structure give rise to move to more positive value and the lattice parameters were monotonously decreased, calculated by (220) peaks of XRD spectra, with increasing the contents of Fe in the nanoparticles. (Figure 3.8) The other peaks were observed in XRD spectra of the PtFe_MS nanoparticles, especially in high contents of Fe species, *i.e.*, Pt1Fe2_MS and Pt1Fe3_MS. (Figure 3.8) It has been reported that the transformation of crystal structures, the Pt1Fe1 fcc into the anisotropy face-centered tetragonal (*fct*), take place exclusively at the temperature, > *ca.* 360 °C, under a flow of 5 vol% H_2 in Ar.[58] In our experimental condition, the annealing temperature below the

reported transition temperature, 300 ^{o}C, was not enough to take place this transformation. Therefore, the additional peaks reflected the formation of the oxidative Fe phase originated from excess amount of Fe not to be incorporated in PtFe structure rather than the superlattice of *fct*. It is worth pointing out that the Pt_1Fe_1 *fcc* crystallinity of the PtFe nanoparticles was obtained by the heat treatment. The electronic structure of PtFe nanoparticles have been investigated by means of the synchrotron based XANES at Pt L_3 edge. According to the theory, the d-metal group exhibits catalytic activity from the frontier d-band, which has a narrower band width relative to the frontier s-band, due to the small coupling matrix between d-orbitals.[6] Therefore, the frontier d-band structures of Pt in PtFe nanoparticles, considered as the only active center, would be characterized such as the d-band vacancy, so as to scrutinize their electrocatalytic activity. Mansour and co-workers have reported that the d-band vacancy was estimated by the difference intensity of Pt L edge, so-called white line.[59] Because the transition probability of Pt L_3 edge is large enough than that of L_2 edge,[60] the vacancy of d-band could be assured by the sharp peak at E_0 = *ca*. 11,564 eV of XANES spectra for Pt L_3 edge resulting from the $2p_{3/2}$ to 5d orbital, allowed electron transition. (Figure 3.7(b) and (c)) The changes of d-band occupancies were negligible in case of the PtFe_RS nanoparticles regardless of their composition. This result inferred that Fe species cannot alter the d-band structure for Pt corresponding with the crystallographic analysis, *i.e*., the phase separation of Pt and Fe species for the PtFe_RS. As shown in Figure 3.7(c), however, intensities of the white line was gradually

decreased with increasing the ratio of Fe to Pt for heat-treated PtFe nanoparticles in the order, Pt1Fe3_MS < Pt1Fe2_MS < Pt1Fe1_MS, consistent with X-ray diffraction results including lattice parameters. The previous reports have suggested that the unfilled d-states be dependent on the extent of alloying.[38, 61] The variation in the intensity of the Pt L_3 edge is attributed by the reduction of the d-band vacancy, as a consequence of altering electronic structures by interaction of Fe into Pt throughout the formation of PtFe *fcc* structure. Hence, we expected that two types of nanoparticles would show the different aspects of the electrocatalytic activity for the ORR with the different contents of Fe species resulting from the diffraction spectra and the characterization of d-band vacancy.

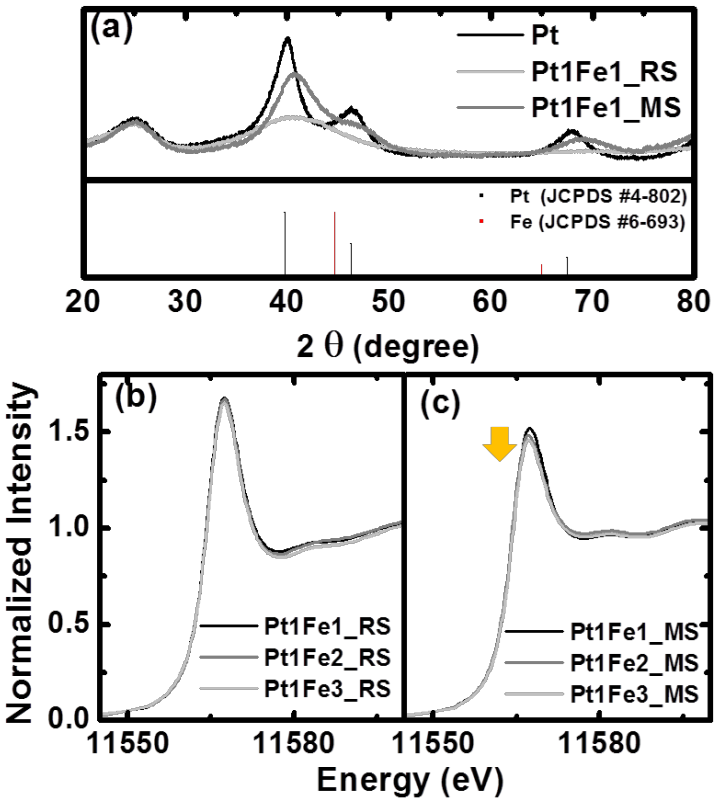

Figure 3.7. (a) HRPD patterns of Pt, Pt1Fe1_RS, and Pt1Fe1_MS at a wavelength 1.5490Å in 9B beam line of Pohang Light Source-II (PLS-II, 3GeV). X-ray absorption near-edge structure of Pt L_3 edge (E_0 = 11,564eV) of (b) PtFe_RS and (c) PtFe_MS nanoparticles in 8C beam line of PLS-II.

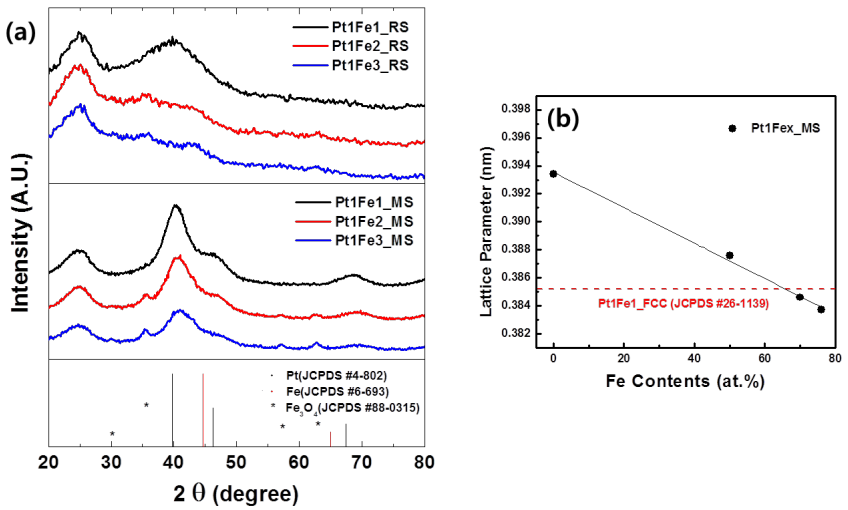

Figure 3.8. (a) X-ray diffraction patterns of PtFe nanoparticles and (b) calculated lattice constant of Pt1Fex_MS (x = 1, 2, and 3) from (220) peaks.

3.1.3. Electrochemical Measurements

To characterize the electrochemical property of the PtFe nanoparticles, we carried out the measurement in 0.1 M $HClO_4$, where the specific adsorption is insignificant during the given potential region for investigation in their intrinsic activities.[22] The CVs were depicted in Figure 3.9. Since the pre-cyclic voltammetry was conducted before records (0.05~1.05 V for 100 scans), most of the unstable species on the surface including Fe, oxidized Fe were etched away under the electrochemical environment, both high acidity and applied potential. Stamenkovic et. al. found that Fe dissolved from the surface layer when Pt-Fe film was immersed in 0.1 M $HClO_4$ from Auger electron spectroscopy and low-energy ion scattering results, as a result of Pt-skeleton surface.[20] For the PtFe_RS, the current density, normalized by the amount of the loaded Pt, at the underpotentially deposited hydrogen (H_{upd}) region (E < *ca*. 0.4 V), makes difference each sample, that is, the peak area was gradually increased in the order, Pt1Fe1_RS < Pt1Fe2_RS < Pt1Fe3_RS. Considering that the electrochemical properties of H_{upd} region were mainly reflected on that of Pt, the only active center, the variation was associated with the dissolution of the passivated layer of the Fe-rich surface. Because the Fe-rich surface was developed by the preferential interaction, Fe-OOC, the Pt inside nanoparticles was exposed to interface between the catalyst and the electrolyte after the removal of the Fe-rich surface. It is plausible that this trend might be related with the particle size under the electrochemical environment consistent with our structural characterization.

Interestingly, the shape of H_{upd} region peaks were quite similar that of the Pt electrocatalyst. (Figure 3.10) Recently, it has been reported that the adsorption properties including hydrogen were significantly altered by alloying of Pt.[62] It is confirmed that Fe is neglect interaction with Pt, resulting from PtFe alloyed phase was not formed by preferential interaction between Fe-OOC, as shown in Figure 3.1. The curve features of CVs of the PtFe_MS were dissimilar to PtFe_RS nanoparticle. In case of PtFe_MS nanoparticles, the H_{upd} region demonstrated the different features compared to pure Pt nanoparticles. Also, the peak area was not significantly tailored for each electrocatalyst. This means that a stable surface with the mixed Pt-Fe phase was formed as discussed above. CO stripping curves correspondingly supported the changes in the surface composition of nanoparticles. Figure 3.9 (right) depicted the oxidation current of CO desorption on the surface of nanoparticles. The completion of CO adsorption was assured by measuring the displacement current ($Pt\text{-}H_{upd} + CO \rightarrow Pt\text{-}CO_{ad} + H^+ + e^-$) to zero. Coinciding with the CV, the area was decreased in the order, Pt1Fe3_RS < Pt1Fe2_RS < Pt1Fe1_RS, with the similar shape of curves. The surface structure of PtFe_RS was reconfirmed by the similar peak shapes regardless of the bulk composition, directly correlated with the surface structure of nanoparticles.[63] Once the Pt-Fe mixed surface was formed, the peak shape and the on-set potential were changed with respect to the bulk composition. It is noteworthy that information for the surface structure could be provided by the electrochemical technique, a surface-sensitive tool.

The polarization curves of the ORR were measured with the saturated O_2, as shown in Figure 3.11. At a mixed kinetic diffusion controlled region, E > 0.7 V, curves showed parallel features consistent with the former observation. The overpotential of the ORR is originated from high binding with oxygen containing intermediate species such as OH^{2-} and O^{2-}.[64] It has been stated that the intrinsic activity for the ORR was enhanced by introducing the 3d group metal into Pt matrix to alter the interaction of intermediate species by means of downshift in the frontier d-band.[6] Evidently, the PtFe_RS exhibited comparable curve features irrespective of their composition, which is in line with our expectation. The interaction between Pt and Fe species was negligible due to the formation of the Fe-rich surface structure. Unlike PtFe_RS nanoparticles, the structural change of PtFe gave rise to the variation in the ORR activity for the PtFe_MS nanoparticles, in descending order, Pt1Fe2_MS > Pt1Fe3_MS > Pt1Fe1_MS. To elucidate the difference in the ORR activity, we measured the aspect of the Fe dissolution after the electrochemical reactions using an ICP-AES. As shown in Table 3.1, the bulk composition of nanoparticles was drastically deviated from the bulk one by the electrochemical dissolution. Interestingly, the Fe dissolution ratio of Pt1Fe2_MS was smallest among other heat-treated samples after the electrochemical condition. Some studies have found that the ORR activity of Pt_xNi_{1-x} nanoparticles were corresponded with the residual Ni contents after the dissolution of non-noble species (Ni) in electrochemical environment.[40, 65] Also, we recall that CO oxidation current of Pt1Fe2_MS at the prepeak

region, E < *ca*. 0.6 V, associated with surface defect sites of Pt nanoparticles,[63, 66] strong interaction with oxygen containing species resulting in sluggish kinetics of the ORR,[67] was smaller than other samples. This result might be related with the low extent of dissolution of Fe species, *i.e*., the formation of electrochemically stable PtFe structure. Therefore, it can be carefully concluded that the enhanced ORR activity of Pt1Fe2_MS was originated from the formation of the electrochemically stable structure relative to other heat-treated nanoparticles.

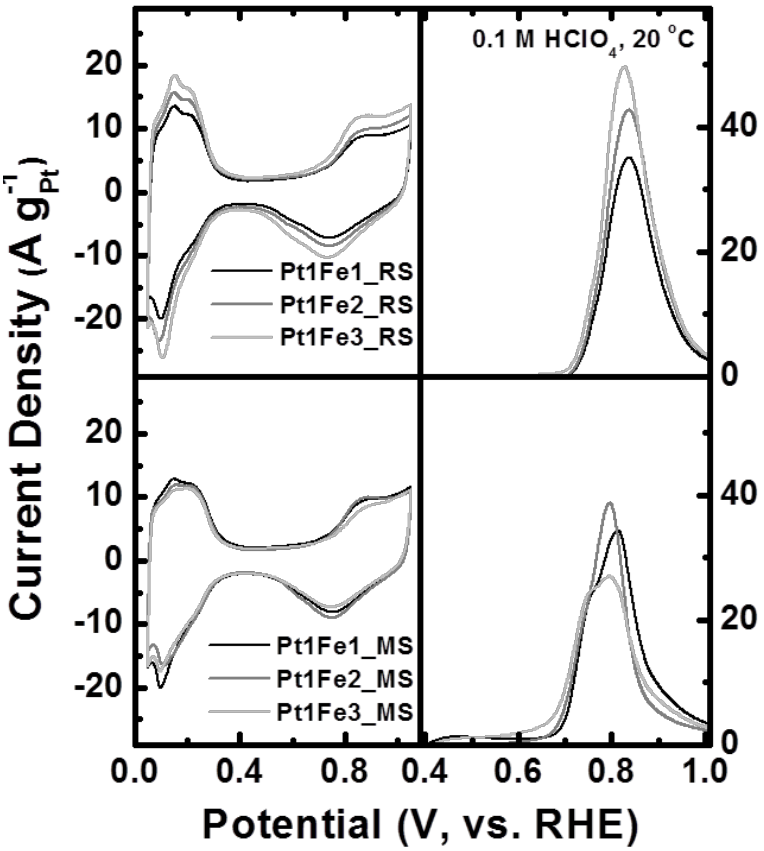

Figure 3.9. Cyclic voltamograms (Left) and CO stripping curves (Right) of the PtFe_RS (Top) and the PtFe_MS (Bottom) nanoparticles in 0.1 M $HClO_4$. (Left) Adsorption of CO was carried out at the potential 0.05 V (vs. RHE) in a flow of high purity CO (99.99+%). All measurements were conducted in a saturated Ar (99.999%) at 20 ^oC.

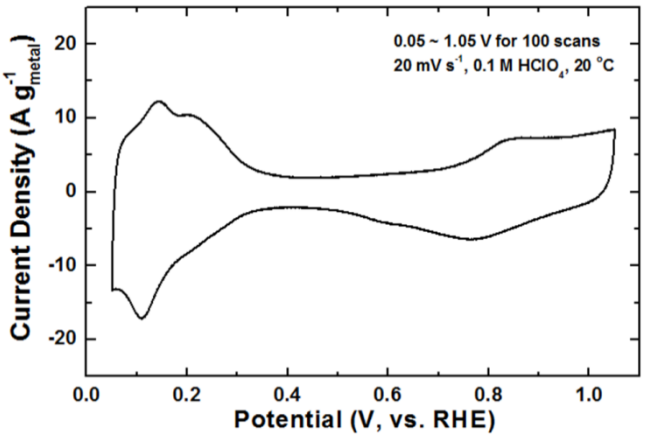

Figure 3.10. Cyclic voltamograms of Pt in a saturated Ar with a scan rate, 20 mV s^{-1} in 0.1 M $HClO_4$. All measurements were conducted in a saturated Ar (99.999%) at 20 ^{o}C.

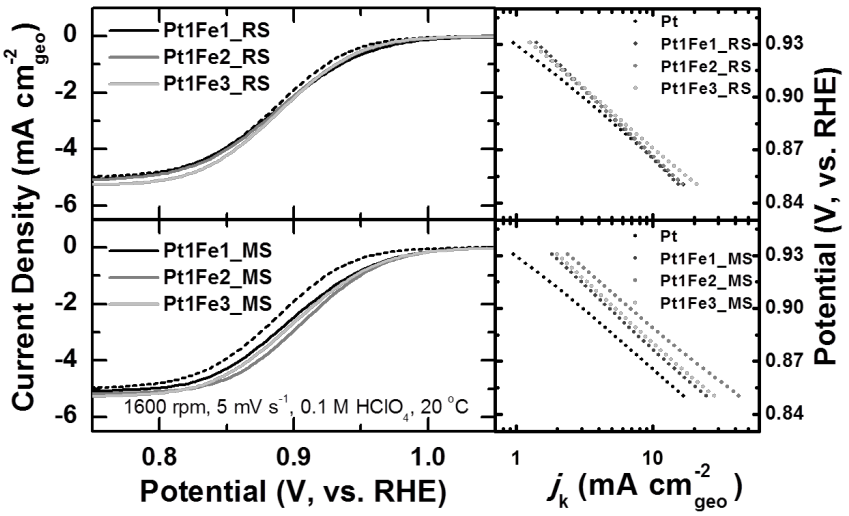

Figure 3.11. Polarization curves (Left) and Tafel plots (Right) for the ORR of the PtFe_RS (Top), the PtFe_MS (Bottom), and Pt (Dotted line). All measurements were conducted at rotation speed, 1600 rpm, in a saturated O_2 (99.995%) at 20 ^{o}C.

3.2. As-Prepared State: Pt-Oleylamine Nanoparticles

3.2.1. Physical and Electrochemical Properties

We assembled Pt_OA ensembles by simply mixing both organic molecules and Pt/C (Johnson Matthey Co., HiSPEC^{TM} 9000, 60 wt.%) with the different molar ratio of OA to Pt: 0, 0.1, 0.3, and 0.5, denoted as Pt, Pt_OA01, Pt_OA03, and Pt_OA05, respectively. Details of the experimental procedure are provided in Experimental section. As shown in Figure 3.14, the electrochemical active surface area (ESA) calculated by underpotentially deposited hydrogen (H_{upd}) region, E < 0.4 V, gradually decreased with an increasing amount of OA. The relative ESA associated with the surface coverage of OA, obtained dividing the ESA of modified electrocatalyst (ESA_{Pt_OA}) by that of the unmodified form (ESA_{Pt}), i.e., ESA_{Pt}/ ESA_{Pt_OA} became samller with increasing the amount of OA. (Table 3.2 and 3.3) Also, the amount of adsorbed OA was confirmed by elemental analysis of C and N. (Figure 3.13) It is noted that decrease of coverage in the order of the initial amount of OA means the surface of Pt was still covered with OA under the electrochemical environment after cycling steps. The activity of ORRs was measured by a hydrodynamic method using a rotating disc electrode (RDE) in saturated O_2 at 20 ^{o}C after pre-cycling step. OA modified electrocatalysts displayed markedly much more facile kinetics at a mixed diffusion-kinetic controlled region (E > 0.7 V), compared to the unmodified electrode, Pt. (Figure 3.14) A reaction rate or current of the

ORR (j) is determined by equation:

$$j=nFKc_{O2}\,(1-\Theta_{ad})^{x}\exp(-\beta FE/RT)\exp(-\gamma \Delta G_{ad}/RT)$$

where n, F, K, c_{O2}, R, x, β and γ are constants, E is the applied potential and T is temperature.[20] The Gibbs energy of adsorption (ΔG_{ad}) for reaction intermediate of oxygen can be tailored according to the design of the electrocatalysts and total surface coverage (Θ_{ad}) due mainly to the spectator species including the adsorption of anions and hydroxyl species. Therefore, enhancement of oxygen reduction reactivity can be achieved by altering these parameters. The alteration can be accomplished by changes in the electronic structure of the frontier d-band (ΔG_{ad}, Θ_{ad}) and by control of the adsorption of spectator species (Θ_{ad}). To clarify these effects, we investigated the d-band characteristics by means of synchrotron based photoelectron spectroscopy (PES) and X-ray absorption fine structure spectroscopy (XAFS). Also, the comparison of activity between electrolytes was investigated, either by the existence of specifically adsorbing anions (0.1 M $HClO_4$ + 0.1 M H_3PO_4) or not (0.1 M $HClO_4$).

Table 3.2. ESAs and surface coverage from CVs in 0.1M $HClO_4$.

0.1M $HClO_4$	Pt	Pt_OA01	Pt_OA03	Pt_OA05
ESA ($m^2\ g^{-1}_{Pt}$)	19.0	17.9	16.9	13.5
Coverage	1	0.94	0.89	0.71

Table 3.3. ESAs and surface coverage from CVs in 0.1M $HClO_4$ + 0.1M H_3PO_4.

0.1M $HClO_4$+0.1M H_3PO_4	Pt	Pt_OA01	Pt_OA03	Pt_OA05
ESA ($m^2\ g^{-1}_{Pt}$)	20.3	19.2	17.4	14.2
Coverage	1	0.95	0.86	0.70

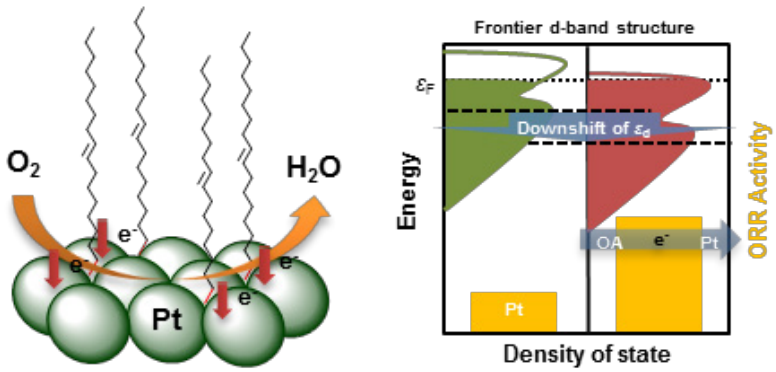

Figure 3.12. Schematic presentation of tailoring d-band structure by the surface capping organic molecules.

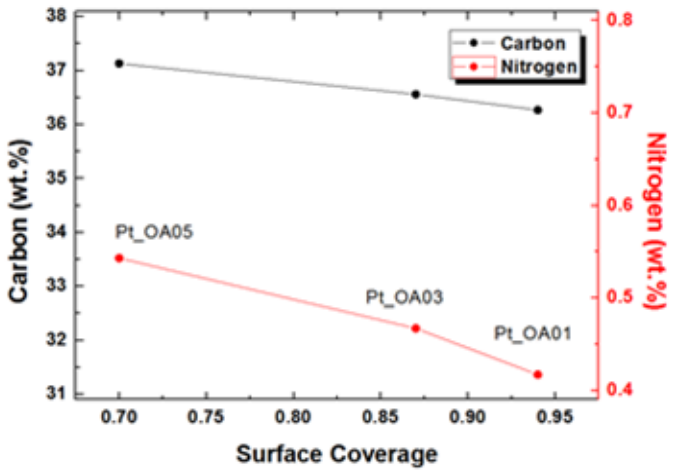

Figure 3.13. Elemental analysis of OA modified Pt nanoparticles: Carbon, Nitrogen.

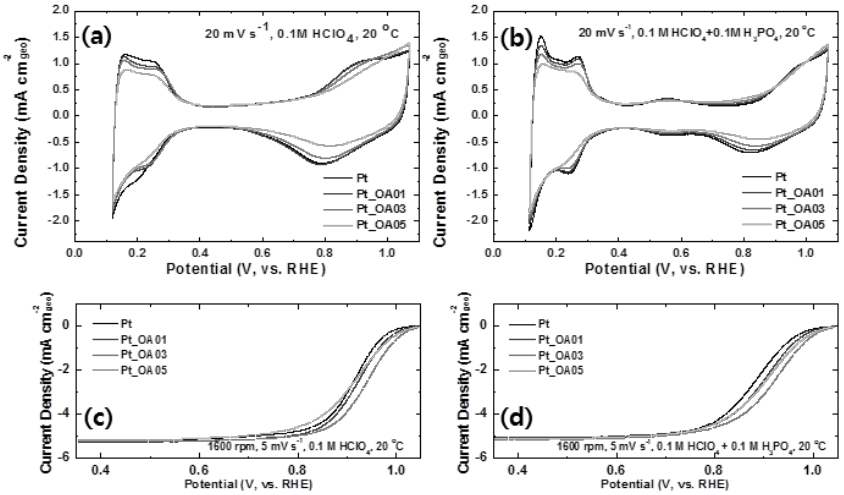

Figure 3.14. Cyclic voltamograms (CVs, top) and polarization curves (ω = 1600 rpm) of the oxygen reduction reaction (ORR, bottom) of Pt/C and OA modified Pt/C in 0.1M $HClO_4$ ((a) and (c)) and 0.1M $HClO_4$ + 0.1M H_3PO_4 ((b) and (d)). All measurements were performed at 20 ^oC in a saturated Ar (99.999%) or O_2 (99.995%).

3.2.2. d-Band Structure of Pt-OA Nano-Catalysts

We characterized the frontier d-band structures of OA modified electrocatalysts using synchrotron sources from Pohang Light Source-II (PLS-II, 3 GeV). The d-band center (ε_d) is one of the most feasible descriptors to estimate activity of oxygen reduction on the Pt surface.[68] The ε_d was calculated from valence band region (ca. -10 eV relative to ε_F) using synchrotron based PES.[69-70] (Figure 3.15(a) and Table 3.4) Interestingly, the addition of OAs produced a lower ε_d relative to unmodified Pt, proportional to the surface coverage, as reported for Pt alloys.[20-21, 71-72] The same tendency of change in the d-band structure induced by OAs was also confirmed by X-ray absorption near-edge structure (XANES) of Pt L_3 edge, the so-called white line, electron transition from $2p_{3/2}$ to unoccupied 5d states. As shown in Figure 3.15(d), the white line intensities of the Pt L_3 edge declined to some extent for modified electrocatalysts; i.e., electrons of the 5d state were more occupied than those in the unmodified state.[73] The alteration of the d-band structure takes place by increasing electron density in the frontier d-states of Pt, and causes downshift of the ε_d, consistent with valence band analysis from PES. This shift of d-band structures might be associated with a geometric effect or an electronic effect. When Pt experiences either tensile or compressive strain, the overlap of the Pt d-state can be altered, so the width of d-band is either wider or narrower. As a consequence, the d-band energy shifts to maintain constant electron filling. For example, compressive strain induced

at the Pt surface leads to the formation of highly overlapped d-states and a downshift of ε_d.[68] To confirm the geometric effect, Pt-Pt distance (R-spacing) was measured using extended X-ray absorption fine structure (EXAFS).[74] Pt-Pt distance was seldom altered regardless of both surface coverage of OAs and d-band structure (Figure 3.15(b)). This result indicated that geometric effect could not be considered as a modification of frontier d-band structure, but instead an electronic effect involving the donation of electrons from organic species, OAs, toward Pt nanoparticles. It is plausible that electron transfer from OAs to Pt is based on a nano-sized effect, i.e., Pt exhibits electron accepting properties from surface capping organic materials at < 7 nm in size, whereas donating properties are evident at > 25 nm.[75] Figure 4 depicts the relationship between the improvement factor of ORRs, calculated by dividing the specific kinetic current density of modified electrocatalyst ($j_{k,\,Pt\_OA}$) by that of the unmodified form, ($j_{k,\,Pt}$) and the difference in ε_d ($\Delta\varepsilon_d$) relative to unmodified Pt in the different electrolytes: 0.1 M $HClO_4$ and 0.1 M $HClO_4$ + 0.1 M H_3PO_4. A plot exhibited a classical volcano-like curve obeying Sabatier principle,[76] which states the maximum catalytic activity is determined by an optimal interaction between a reactant and a catalyst. Because ε_d is directly associated with interaction for d-band metal, a negative shift of ε_d indicates that the intermediate species of ORRs weakly interacted with electrocatalysts and the kinetics are facile. Pt_OA03 demonstrated the highest electrocatalytic activity at $\Delta\varepsilon_d$ of ca. -0.3 eV, which corresponded with previous experimental results for Pt_3M alloys.[20-21, 72] Interestingly,

other amine terminated organic molecules such as aniline (AN, $C_6H_5NH_2$) and hexamethylenediamine (HMDA, $NH_2(CH_2)_6NH_2$) also showed the enhancement of the ORR kinetics compared to unmodified Pt nanoparticles.(Figure 3.17) Therefore, it is worth pointing out that nitrogen included organic molecules can induce tuning of the electronic structure of Pt nanoparticles for ORRs as a promoter. (Figure 3.12)

Table 3.4. The d-band center calculated by valence band spectra from PES.

(eV vs. E_F)	Pt	Pt_OA01	Pt_OA03	Pt_OA05
d-band center (ε_d)	-3.18	-3.24	-3.49	-3.58
$\Delta\varepsilon_d$ (ε_{d,Pt_OA}-$\varepsilon_{d,\ Pt}$)	0.00	-0.06	-0.31	-0.40

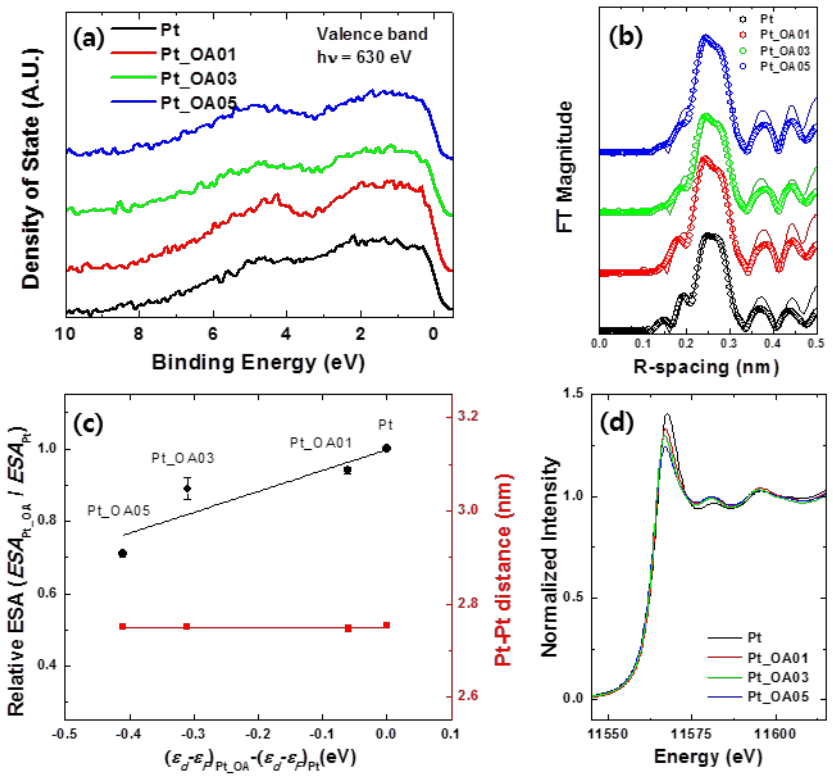

Figure 3.15. (a) Photoelectron spectra of valence band with Shirley background correction at 630 eV, (b) Fourier transform of k^3-weighted XAFS spectra to R-spacing value at Pt L_3 edge (E_0 = 11,564 eV): raw (line) and fitted (bold) data, (c) Relationship between surface coverage of oleylamine (black) and Pt-Pt distance (red) as a function of the difference of d-band center relative to Pt/C, and (d) XANES of Pt L_3 edge of Pt/C and OA modified Pt/C.

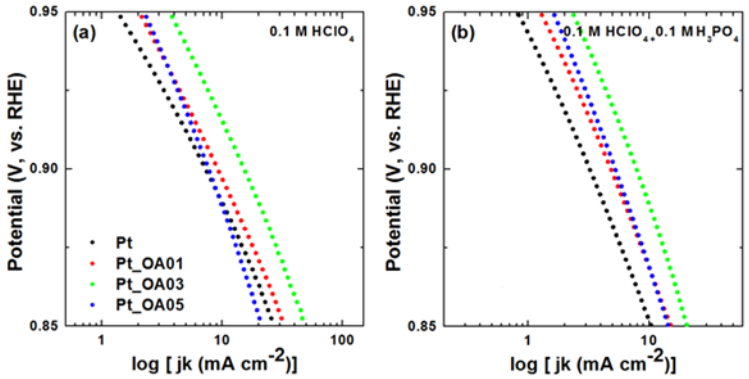

Figure 3.16. Kinetic current density of ORRs in (a) 0.1 M $HClO_4$ and (b) 0.1 M $HClO_4$ + 0.1 M H_3PO_4.

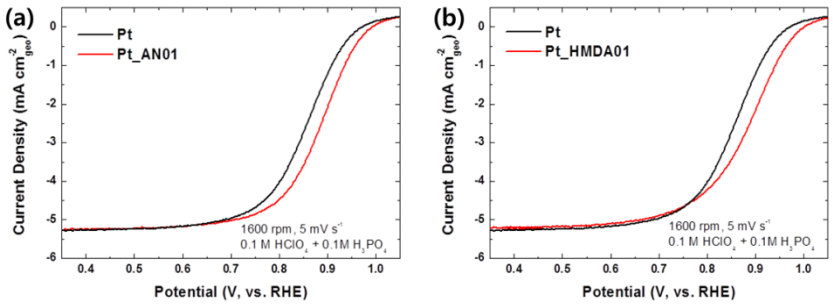

Figure 3.17. Polarization curves of ORR for (a) AN and (b) HMDA in 0.1M $HClO_4$ + 0.1M H_3PO_4 in a saturated O_2 (99.995%).

3.2.3. Adsorption Properties

We investigated the retardation of adsorption of spectator species by bulky organic molecules controlling free sites (1-Θ_{ad}) of electrocatalysts. Surface coverage is determined mainly by spectator species such as anions and OH_{ad}, while O_2 and intermediates including O^{2-} and HO^{2-} relatively very small coverage for ORRs.[24] The adsorption of spectator species hinders ORRs by blocking surface active sites and by altering the adsorption isotherm of reaction intermediates.[77] Without specific adsorption of anions, OH_{ad} was a major spectator species at a mixed diffusion-kinetic controlled region. Polarization curves of ORRs in 0.1M $HClO_4$ (Figure 3.14(c)), in which the specific adsorption of anions is negligible due to a smaller hydration energy,[22] revealed that the slope gradually decreased with increased surface coverage of OAs. This was consistent with the recovery of the intrinsic kinetic value.[77] This may have resulted from retardation of formation of OH_{ad} associated with changes of d-band structure and hindrance of adsorption of OH_{ad} by the initially covered OA species.(Figure 3.14(a), (c)) Otherwise, curves featured a different aspect in the presence of specific adsorption.(Figure 3.14(b), (d)) The activity of ORRs in H_3PO_4 is severely deactivated through adsorption of phosphate anions.[25, 78-82] Because the adsorption of anions occurs at the low potential relative to OH_{ad}, anions occupy most of active sites before formation of OH_{ad}, resulting in positive shift of the on-set potential about formation of OH_{ad} compared to $HClO_4$.(Figure 3.14(a)) The effect of OH_{ad} becomes insignificant and

adsorption isotherm remains nearly constant at a high potential region.[77] Therefore, ORR activity, within the framework of surface coverage, is decisively determined by the anion adsorption onto Pt nanoparticles in H_3PO_4. Improvement factors of the modified electrocatalysts displayed higher values in 0.1 M $HClO_4$ + 0.1 M H_3PO_4 than in 0.1 M $HClO_4$.(Figure 18 and 19) As shown in Figure 3.14(b), the peak at ca. 0.55 V, associated with the phosphate adsorption on Pt(111),[82] was significantly decreased with the increased surface coverage of OA. This can be interpreted as indicative of an allowed low coverage of phosphate anions by lowering the adsorption strength as a result of alteration in the frontier d-band structure. According to Hammer and Nørskov,[68] the narrow d-band could form bonding and anti-bonding states toward adsorbate atoms or molecules, resulting in facilitating surface chemisorption. The theory further posits that as the strength of chemisorption increases, the gap between the spilt-off bonding and anti-bonding states becomes larger. A lower ε_d of the modified electrocatalysts indicates the formation of a weak chemisorption between the Pt nanoparticle and the anion adsorbate. Also, the decreased adsorption of phosphate anion can be attributed to blocking the adsorption of bulky organic species when we carefully considered phosphate preferentially adsorbed on the three-fold site of the Pt surface.[81-82] Recently, the cyanide patterned electrode revealed that the phosphate adsorption could be effectively hindered by the surface species during the ORR.[26] The blocking effect was also confirmed by the inferior ORR activity of organics containing short hydrocarbon chains, AN and HMDA to OA.(Figure 3.17)

Therefore, it is expected that bulky organic species modified electrocatalysts such as OA are more advantageous when applied in a real fuel cell system where specific anion adsorption takes place. (Figure 3.20)

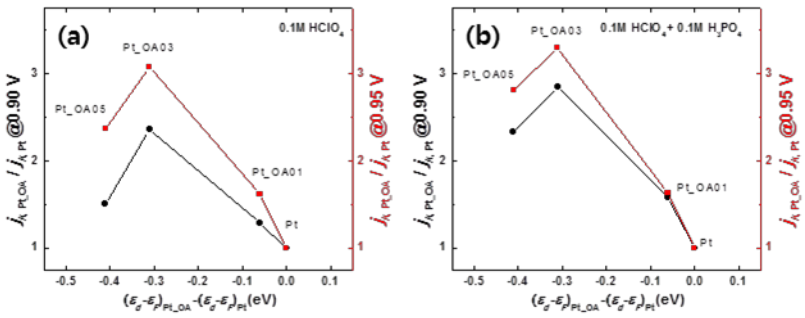

Figure 3.18. Improvement factors ($j_{k,Pt\_OA}/j_{k,Pt}$) relative to Pt/C as a function of the difference of d-band center ($\Delta\varepsilon_d$, $(\varepsilon_d-\varepsilon_F)_{Pt\_OA}$- $(\varepsilon_d-\varepsilon_F)_{Pt}$) in (b) 0.1M $HClO_4$ and (c) 0.1M $HClO_4$ + 0.1M H_3PO_4 at 0.90 (black) and 0.95 V (red) vs. RHE. The specific kinetic current densities were calculated by ESAs.

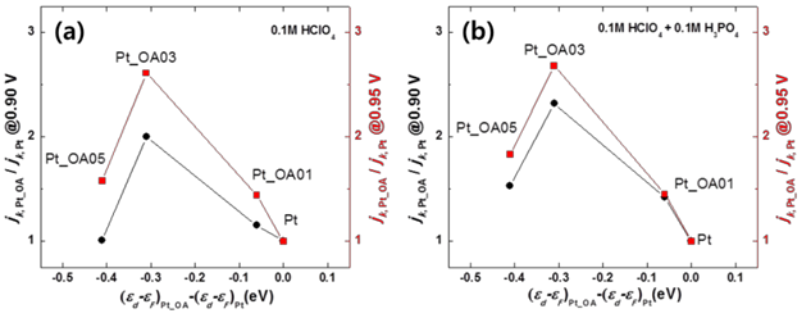

Figure 3.19. Improvement factors relative to Pt/C as a function of the difference of d-band center in (a) 0.1M $HClO_4$ and (b) 0.1M $HClO_4$ + 0.1M H_3PO_4.

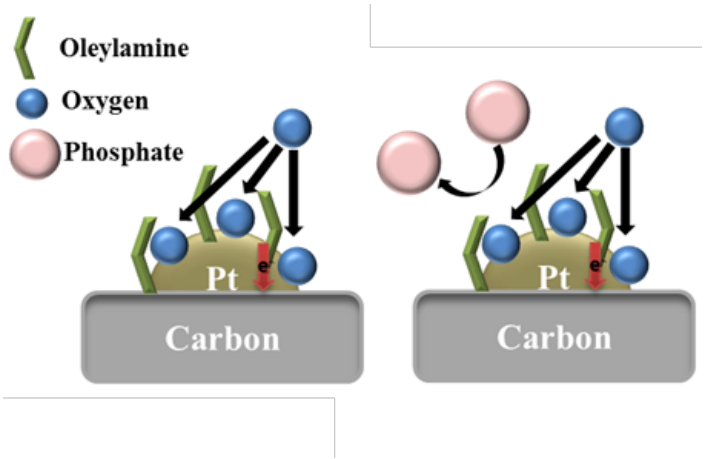

Figure 3.20. The third body effect of oleylamine for hindering adsorption of phosphate ions.

3.3. Post-Treatment: Pt_1Ni_1 and Pt_2Ni_1 Nanoparticles

3.3.1. Effect of Temperature: Characterization

As shown in Figure 3.21, carbon supported PtNi nanoparticles were prepared via the colloidal reduction method. To control structural ordering of bimetallic phase, we carried out nanoparticles were thermally annealed under a reductive atmosphere, that is, a flow of H_2/Ar (5/95 vol%) at the different temperature, 300 and 700 ^oC. Because the mobility of individual metallic atoms is sufficient to move around on the surface of nanoparticles, when to apply the thermal energy, the intermetallic structures gives rise to be reconstructed toward the stable phase such as the intermetallic ordering and the reorientation of surface facet. According to previous calculations, the formation of Pt-Ni bulk alloy was energetically favorable compared to Pt.[83-84] Some studies demonstrated that the intermetallic ordering for Pt-Ni, i.e., increases in the extent of alloying, takes place during the heat treatment process. Within the thermodynamic correlation, the surface facets of face-centred cubic (*fcc*) structures including Pt, would be stabilized in the order, (111) < (100) < (110), in accordance with sequence of surface energies.[85-86] The specific facets such as (111) would be easily developed during the thermal annealing.[87] Within the line of our expectation, it was reported PtNi based mesostructured thin films were obtained with the enrichment of (111) facets after thermal annealing at 400 ^oC in a hydrogen-rich atmosphere.[88]

After the thermal annealing, the well-defined PtNi nanoparticles were formed as shown in Figure 3.22(a) and (b). The particle size distribution showed that the average radius of PtNi nanoparticles were slightly varied with respect to the thermal energy from low-magnification TEM images, that is, *ca*. 2.5 and 2.7 nm for PtNi/C_300 and PtNi/C_700, respectively. It is noteworthy that the particle size, affected to the electrochemical reaction, was not significantly agglomerated after the heat treatment. A typical fcc structures were exhibited from high-resolution TEM images and reduced fast Fourier transform (FFT) spectra for an individual nanoparticle. Each nanoparticle maintained the bulk atomic composition during the thermal annealing process,$Pt_1Ni_{1.1}$ and $Pt_1Ni_{1.1}$ for PtNi/C_300 and PtNi/C_700, respectively, within the error range of ICP-AES.

Like other Pt-3d metal alloys, it is known that the face-centred tetragonal (*fct*) of Pt and Ni were developed at the high temperature, > 645 ^{o}C.[89] To clarify this transformation, the crystallographic analyses were performed using the high-resolution powder diffraction based on the synchrotron-based X-ray source. (Figure 3.22(c))Interestingly, peaks associated with the space group, *P4/mmm*, were not detected even at the high temperature, 700 ^{o}C.[90] It was also observed that the tetragonal transition was not generated in case of PtNi nanoparticles even at the more high temperature, 900 ^{o}C.[91]Instead, diffraction patterns of a typical *fcc* structure of Pt (space group, Fm-3m) at 40^{o}, 46^{o}, and 68^{o},[92] corresponded to (111), (200), and (220), were positively shifted as incorporating Ni atoms into the Pt structure. This means the Pt-Pt lattice distance in *fcc* structure of Pt is compressed by the

Ni phase, relatively small size, due to the structural ordering during the heat treatment. The extent of peak shifts was higher when to increase the thermal energy. The quantitative analyses for the intermetallic ordering between Pt and Ni species were shown in Table 3.5. As discussed above, the degree of alloying was varied with the temperature, that is, 78 and 94% for PtNi/C_300 and PtNi/C_700, respectively. Also, the average particle size, calculated by Scherrer' equation for (220) peak,[93] was quite matched with the TEM measurement. It is worthy pointing out that the particle size cannot be significantly affected to the electrocatalytic activity, because the size of the reference nanoparticle, Pt/C, was the similar value to that of the prepared samples.

The X-ray absorption spectra of Pt L_3 edge were measured to obtain electronic and structural information for PtNi nanoparticles. (Figure 3.22(d)) In the Pt L_3 near-edge region, intensities of the white line, electron transition from $2p_{3/2}$ to 5d orbital, d-band vacancy was reduced in the order, PtNi/C_300 <PtNi/C_700. This result is correlated with the extent of structural ordering, *i.e.*, electronic interactions from Ni to Pt species occur more effectively considering negligible size effect.[73] Extended X-ray absorption fine structure (EXAFS) featured the different aspects as the thermal energy. Particularly, the coordination numbers of Pt-Pt and Pt-Ni were demonstrated inverse trends, that is, more structural ordering is proceeded at the high annealing temperature as discussed above.

To clarify the reorientation of surface facet, we carried out the electrochemical techniques such as CO oxidation and irreversible Bi

adsorption. Previous studies have stated that the oxidation properties of adsorbed CO on the surface of Pt-based nanoparticles are related with the surface facet.[63, 94-95] The first peak of CO stripping curve, at *ca*. 0.7 V, is connected with the oxidation current of (111) facet.[63, 95] To separate ratio of (111) facet in nanoparticles, we deconvoluted the oxidation peak into two fitting curves. (Figure 3.23(a) and (b)) Also, we conducted another measurement, the irreversibly adsorbed Bi on (111) facet of Pt at *ca*. 0.62 V, to confirm reorientation of the surface direction.[96-99] (Figure 3.23(c)) These two electrochemical techniques indicated the similar ratio of (111) facet within 5%. Concerning differences of surface energies for facets, the ratio of (111) facet was significantly increased after the heat treatment, in the order, PtNi/C_700 >PtNi/C_300, as expected. These surface reconstructions including the surface ordering and reorientation of surface facet were summarized in Figure 3.24(c). It is posited that the thermal energy gives rise to the intermetallic ordering and the (111) direction reorientation, proportional to the annealed temperatures.

Table 3.5. Structural information from the HRPD measurements.

Samples	2θ of (220) (degree)	FWHM	Particle Size (nm)	Lattice Parameter (Å)	Extent of Alloying (%)
Pt/C	67.86	3.62	2.66	3.94	N/A
PtNi/C_300	70.68	3.91	2.51	3.79	78
PtNi/C_700	71.30	3.41	2.88	3.76	94

Table 3.6. EXAFS fitting results of PtNi nanoparticles.

Samples	R-spacing (nm)			Coordination Number			R-Factor
	Pt-Pt	Pt-Ni	Pt-O	Pt-Pt	Pt-Ni	Pt-O	
PtNi/C_300	2.69	2.62	1.98	4.6	3.0	0.8	0.01
PtNi/C_700	2.68	2.61	1.99	3.3	3.6	0.6	0.01

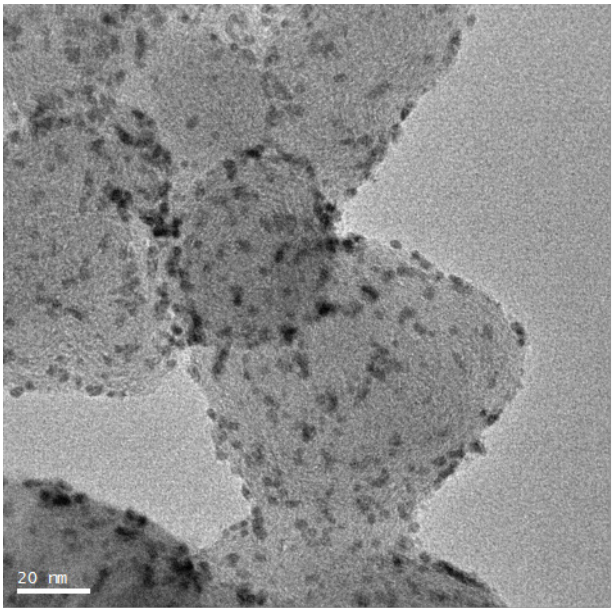

Figure 3.21. TEM images of as-prepared PtNi nanoparticles.

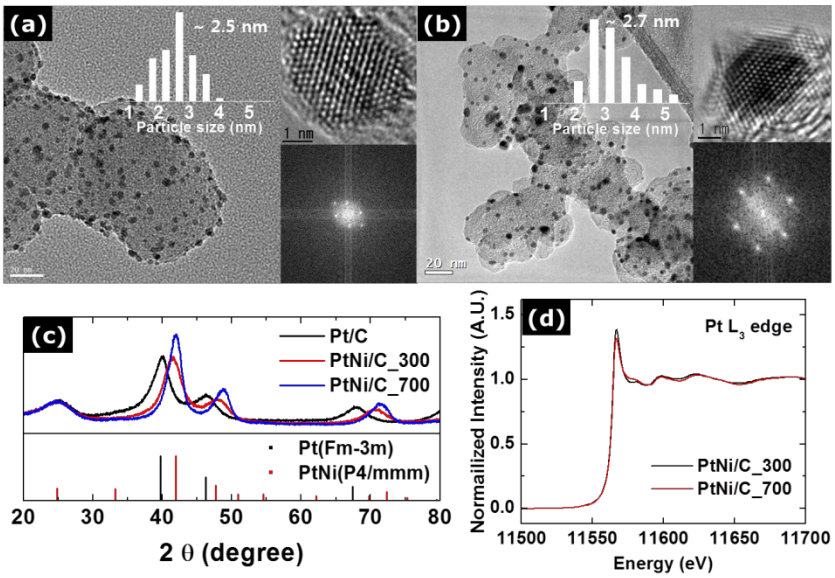

Figure 3.22. TEM images of (a) PtNi/C_300 and (b) PtNi/C_700: Particle size distributions (inset), high resolution images (top right), and their reduced FFT pattern (bottom right). Spectra of (c) high resolution powder diffraction and (d) X-ray absorption spectra of Pt L_3 edge at E_0 = 11,564 eV.

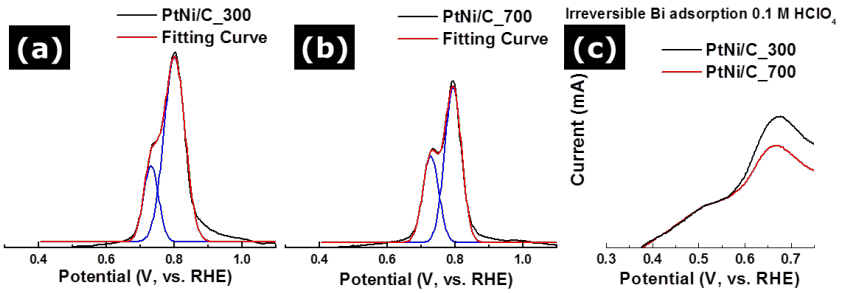

Figure 3.23. Deconvolution of CO stripping peaks for (a) PtNi/C_300 and (b) PtNi/C_700. Oxidation peaks of irreversibly adsorbed Bi on the surface of PtNi nanoparticles. All measurements were conducted in 0.1 M $HClO_4$ at 20 ^{o}C.

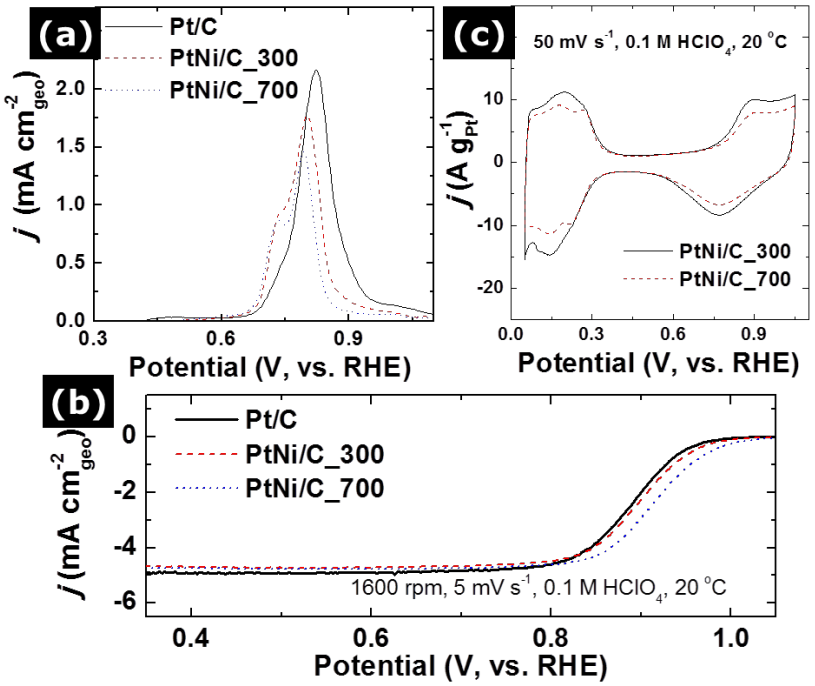

Figure 3.24. (a) CO stripping curves with CO adsorbed surface at 20 mV s^{-1}, (b) polarization curves of the ORR at 5 mV s^{-1} with 1600 rpm, and (c) cyclic voltamograms at 50 mV s^{-1}. All measurements were carried out in 0.1 M $HClO_4$ at 20 ^{o}C.

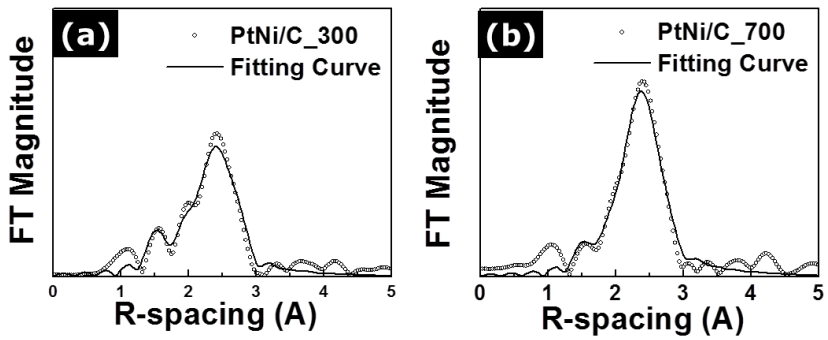

Figure 3.25. Fitting curves of EXAFS spectra using an ARTEMIS software.

3.3.2. Effect of Temperature: Electrocatalytic Activity

The electrocatalytic activity was measured in an acid electrolyte, 0.1 M $HClO_4$, the low extent of the anion adsorption due to large hydration of ClO_4^-.[22] (Figure 3.24) In particular to the ORR for Pt-based electrocatalysts, intrinsic kinetics was decisively determined by adsorption properties on the surface of metal. For the single Pt species, it is favorable to achieve facile kinetics to the ORR that the adsorption strength of reactants and intermediates should be lowered.[64, 84] Alloying Pt with the 3d-metal including Ni can modify the adsorption properties by tuning the d-band structure of Pt through both geometric and electronic way.[100] The specific oriented nanoparticles, especially toward (111) terrace sites, can enhanced the intrinsic kinetics to the ORR.[63, 88] Therefore, the structural properties of PtNi nanoparticles, governed the interaction between Pt and Ni and surface orientation, has primarily importance to the reaction kinetics of the ORR. The polarization curves of the ORR exhibited enhancement of electrocatalytic activity for thermal annealed PtNi nanoparticles compared to referent Pt/C. (Figure 3.24(b)) Trends of activity is consistent with the degree of surface ordering and reorientation as observed in structural characterization. The cyclic voltamograms of the PtNi nanoparticles also showed that the peaks associated with hydroxyl adsorption/desorption, competitive adsorption species derived from water, *i.e.*, $H_2O \leftrightarrow OH(ad) + H^+ + e^-$, in the mixed kinetic-diffusion controlled region, $E > 0.7$ V, were retarded as increasing structural ordering as shown in Figure 3.24(c).

The additional analyses were performed such as C_S-corrected STEM equipped with EDS and XPS after electrochemical measurements to elucidate direct correlation between structural reconstructions and catalytic activities. (Figure 3.28) The dissolution of unstable 3-d metal, Ni, is inevitable due to the harsh condition of electrochemical measurements.[101] The EDS results for the line scanning of Pt and Ni component clearly supported that less reconstructed structure severely suffered from the dissolution of Ni species. Moreover, the quantitative investigation of Pt 4f and Ni 2p XPS spectra revealed that the ratio of the composition of Pt and Ni was $Pt_{1.8}Ni_1$ and $Pt_{3.8}Ni_1$ for PtNi/C_300 and PtNi/C_700, respectively. Considering the heat of formation Pt-Ni, the more reconstructed species can be more stable structure in the electrochemical environment.[83] It has been reported that the residual Ni in PtNi nanoparticles after the dissolution is proportional to the ORR activity.[40, 65] Moreover, we scrutinized the binding energy of Pt $4f_{7/2}$ to elucidate how structural stability, stem from the intermetallic reconstruction, was affected to tuning the electronic structure. The shift of core-level of electronic structure for the d-group metal associated with the frontier d-band structure, influencing the adsorption properties.[102-103] According to the theory, d-band structure of Pt would be tuned toward the negative way to weaken the adsorption strength as consequence of improvement of the ORR kinetics.[6] If the downshift of d-band states occurred, the core-states are suppressed downward resulting in high binding energy.[104] Investigated after electrochemical measurements, the measured electronic structure was directly reflected at environments

where the reaction took place. The binding energy of Pt $4f_{7/2}$, 71.6, 71.7, and 71.9 eV for Pt/C, PtNi/C_300, and PtNi/C_700, respectively, was commensurate to the activity for the ORR. This means that the interaction between Pt and Ni species is more active for the highly reconstructed nanoparticles. We depicted the relationship between activity, binding energy and residual Ni in Figure 3.28(d).

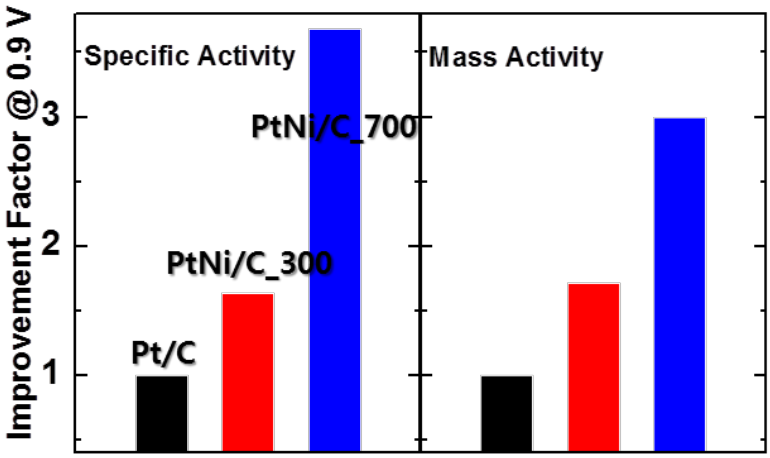

Figure 3.26. Improvement factor (vs. Pt/C) based on specific area (left) and mass (right).

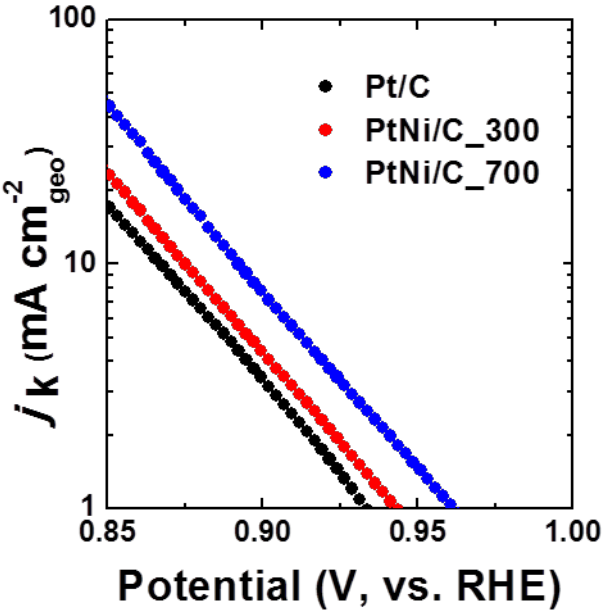

Figure 3.27. Tafel slopes based on the kinetic current (*j*k).

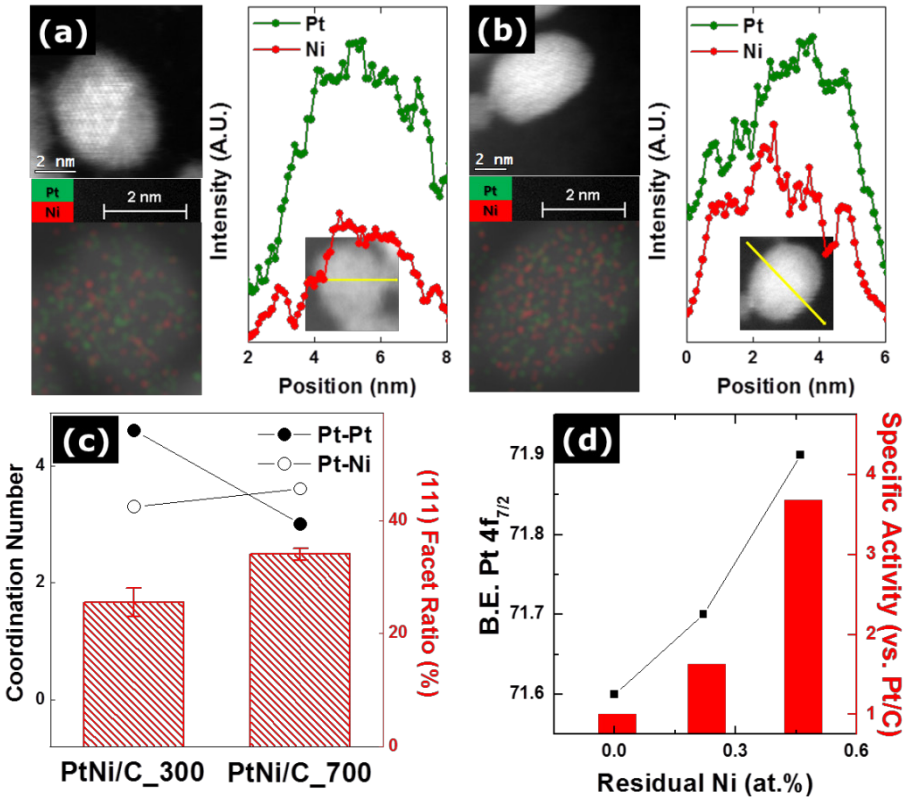

Figure 3.28. Cs corrected STEM images with EDS analysis after electrochemical reactions of (a) PtNi/C_300 and (b) PtNi/C_700, (c) Structural changes of PtNi nanoparticles, and (d) relationship of residual Ni, binding energy of Pt $4f_{7/2}$, and specific activity.

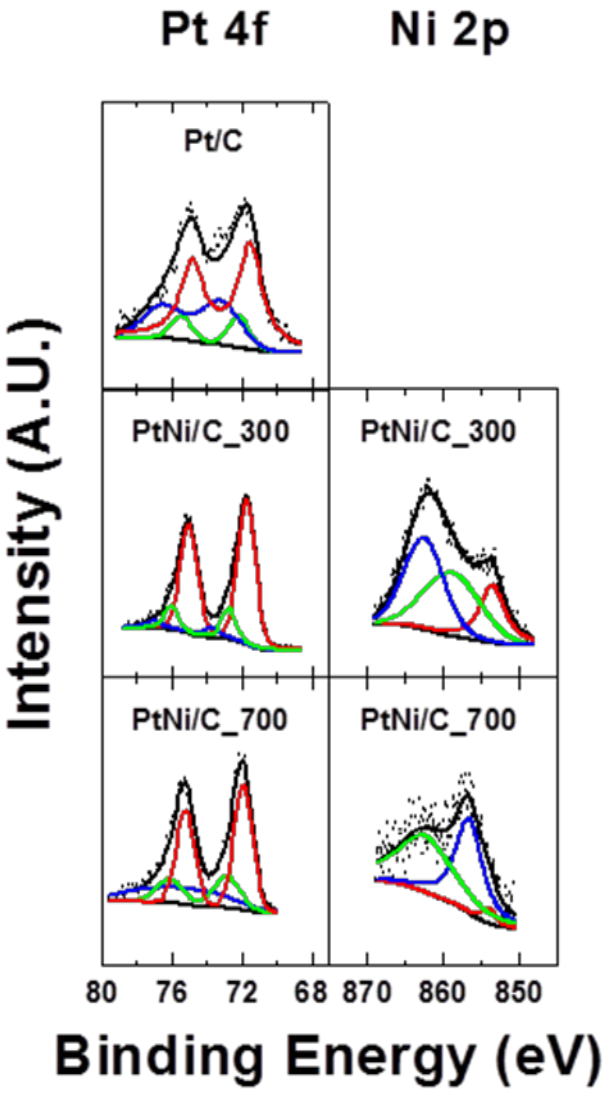

Figure 3.29. X-ray photoelectron spectra of Pt 4f and Ni 2f for PtNi nanoparticles after electrochemical reactions.

3.3.3. Effect of Atmosphere: Characterization

In order to elucidate the effect of heat treatment atmosphere for the ORR, we carried out that PtNi nanoparticles were annealed at three different gases such as Ar, H_2/Ar (5/95 vol%), and compressed air. Physical appearances were examined by TEM image in Figure 3.30(a), (b), and (c). The PtNi nanoparticles were not demonstrated significant changes after annealed in the different gaseous atmosphere. The particle size was estimated by ca. 3.4, 3.5, and 3.3 nm for PtNi_Ar, PtNi_H2, and PtNi_Air, respectively. From ICP-AES measurement, we confirmed that the atomic ratio of Pt to Ni was nearly retained after heat treatment process; $Pt_{1.0}Ni_{0.52}$ (PtNi_AP), $Pt_{1.0}Ni_{0.53}$ (PtNi_Ar), $Pt_{1.0}Ni_{0.53}$ (PtNi_H2), and $Pt_{1.0}Ni_{0.51}$ (PtNi_Air), respectively. As shown in Figure 3.30(d), the XRD patterns were, for some extent, varied with the treated gas. The typical diffraction peaks of a face centered cubic (*fcc*) Pt structure (FM3-M) in scan range were detected at 39.8^o, 46.2^o and 67.5^o, i.e., (111), (200), and (220) facet, respectively. (JCPDS #4-802) During the heat treatment process, Pt diffuse out on the surface of resulting in forming PtNi mixed phase. In case of PtNi_Ar and PtNi_H2, the diffraction peaks were featured similarly, to some extent, the higher angle shift than those of Pt species, i.e., the contraction of Pt lattice, resulting from alloying Pt with Ni. On the other hand, the PtNi nanoparticles annealed by an oxidative atmosphere (PtNi_Air) exhibited somewhat different patterns. Firstly, the peak shift was smaller than PtNi_Ar and PtNi_H2. This result indicated that mixed Pt-Ni phase was not effectively

formed in an oxidative environment. Secondly, the width of peak gave rise to be broader. Considering the peak broadness was directly related with the domain size of crystalline phase, it is likely that the crystallinity of PtNi_Air was significantly decreased during the heat treatment process. Lastly, distinct peaks at 2θ = ca. 35^{o} and 40^{o} were observed for the diffraction pattern of PtNi_Air. According to previous literature,[105] these peaks were corresponded with crystalline facets of β-PtO2 (Pnnm). Therefore, it can be carefully concluded that the mixed Pt-Ni phase were developed successfully in a reductive atmosphere (PtNi_Ar and PtNi_H2), while ineffectively in an oxidative atmosphere (PtNi_Air) due to the formation of oxidized Pt phase.

The polarization curves for the ORR were obtained in the different electrolytes, 0.1 M $HClO_4$ and 0.1 M $HClO_4$ + 0.1 M H_3PO_4. (Figure 3.31) For the high temperature PEMFC, phosphoric acid doped PBI based membrane was generally utilized due to the chemical and mechanical feasibility.[106] In phosphoric acid, unfortunately, Pt based electrocatalysts were severely suffered in surface poisoning by specific adsorption of phosphate anions due to weakly solvated phosphate anions at the operation condition resulting in sluggish kinetic of the ORR relative to that in the perchloric acid.[22] It is important that the ORR activity should be investigated in the presence of specific adsorption of phosphate anions to apply the electrocatalyst to the real system. For that reason, we measured that the ORR activity in two different electrolytes; 0.1 M $HClO_4$ and 0.1 M $HClO_4$ + 0.1 M H_3PO_4, to scrutinize intrinsic activity (the former) and

tolerance in poisoning (the latter). According to the DFT calculations,[64] the ORR activity of platinum based electrocatalysts can be facilitated by decrease in the adsorption strength of oxygen containing intermediate species. Alloying with 3-d transition metals (Ni, Co, Fe etc.) was one of the most common approaches to enhance electrocatalytic activity. The adsorption strength on the surface of Pt was controlled by the frontier electronic states, d-band structure having a narrow band width. For PtNi nanoparticles, the frontier d-band structure of Pt can be tailored by Ni species through both electronic and geometric effect.[20-21] Therefore, the interaction between Pt and Ni is decisively affected on the ORR activity. The polarization curves demonstrated that the interaction was varied with the gaseous atmosphere during heat treatments. The specific kinetic current densities at 0.9 V were improved compared to the reference commercial Pt/C (40 wt%), by the factor, PtNi_Ar > PtNi_H2 > PtNi_Air in 0.1 M $HClO_4$. It is pointed out that the intrinsic activity was effectively facilitated when to be annealed in argon atmosphere. It is noteworthy that activity for the ORR in presence of phosphoric acids showed the same tendency compared with the small adsorption of anions. This fact might originate from that adsorption strength of anions was also affected by the frontier electronic structure of Pt, similar to oxygen containing species. However, the activity of PtNi_Ar was still conserved while that of others was, to large extent, decreased as the addition of phosphoric acid, i.e. enhancement of tolerance in anion adsorption. Cyclic voltamograms featured evidences of the extent of adsorption for PtNi nanoparticles. As shown in Figure 3.32,

the intensity of peaks at ca. 0.55 V and 0.3 V, associated with the adsorption on Pt(111) and Pt(100) was disproportion to the ORR activities.[82] As a result, the tolerance in the anion adsorption was also achieved by Ar atmosphere. As discussed above, the PtNi nanoparticles annealed in compressed air (PtNi_Air) might be expected lower interaction between Pt and Ni due to the lower crystallinity and formation of oxidative species of Pt. However, the variation in activities for heat-treated electrocatalysts in argon and hydrogen were still elusive based on the XRD analysis. The additional characterization and discussion were as follow, investigations of electronic structure.

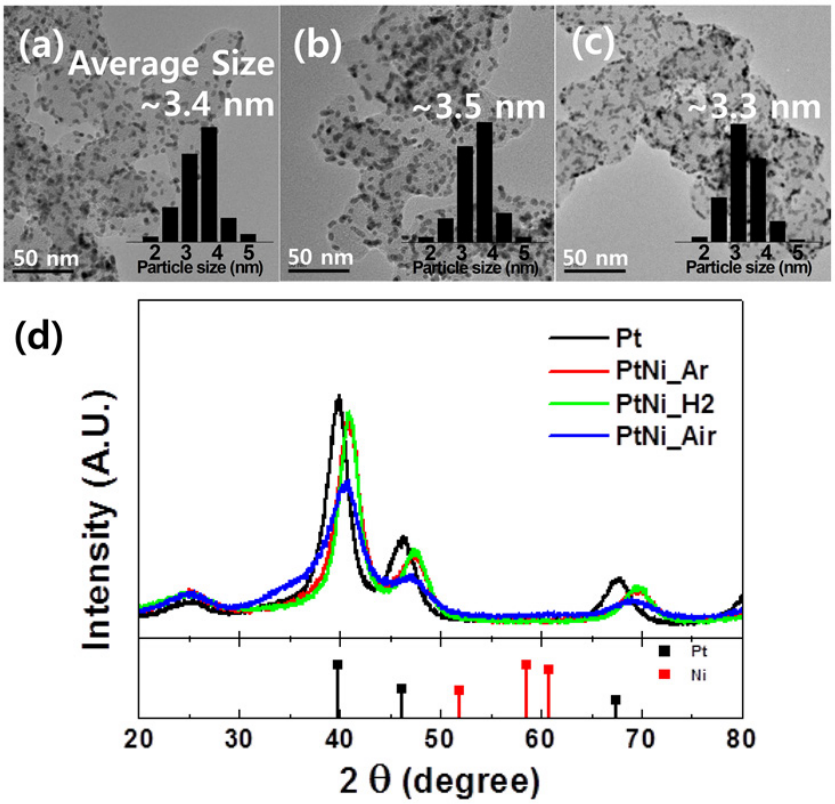

Figure 3.30. TEM images of (a) PtNi_Ar, (b) PtNi_H2, and (c) PtNi_Air and particle size distribution. (inset) (b) X-ray diffraction patterns of PtNi nanoparticles.

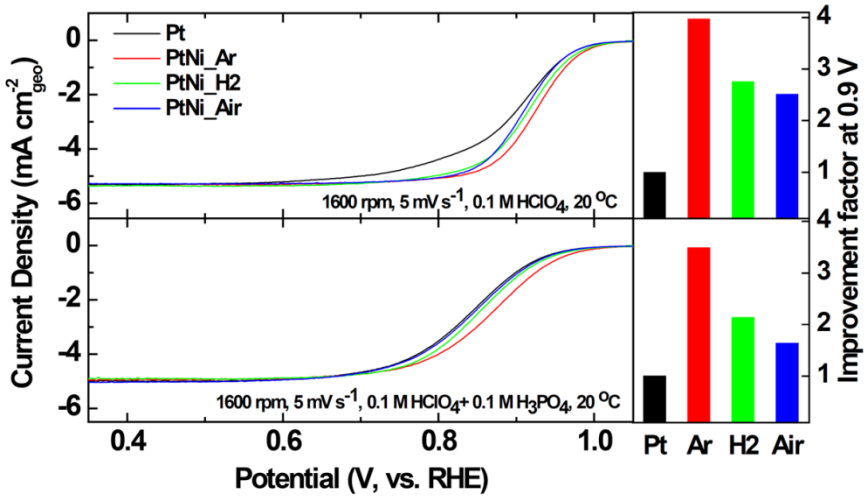

Figure 3.31. Polarization curves of the ORR (left) and the improvement factor at 0.9 V (vs. Pt/C, right) in 0.1 M $HClO_4$ (top) and 0.1 M $HClO_4$ + 0.1 M H_3PO_4. (bottom) All measurements were performed with 5 mV s^{-1} and 1600 rpm at 20 ^oC.

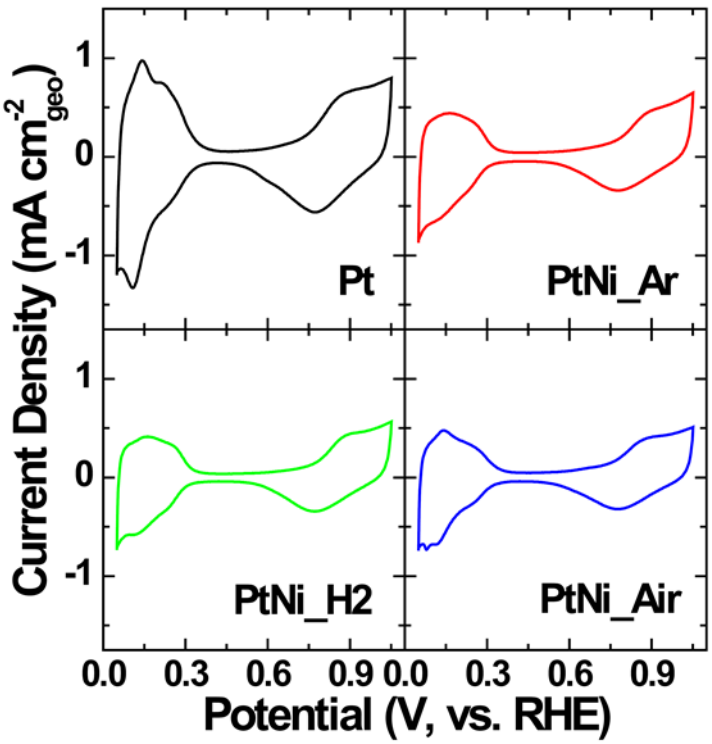

Figure 3.32. Cyclic voltamograms of Pt and PtNi nanoparticles in 0.1 M $HClO_4$ with 20 mV s^{-1} at 20 ^{o}C.

3.3.4. Effect of Atmosphere: Electronic Structures

To clarify the electronic structure of nanoparticles, we measured X-ray spectroscopic technique. XANES spectra of Pt L_3 (E_0 = 11,564 eV) and Ni K (E_0 = 8,333 eV) edge were examined in Figure 3.33. The absorption edge was directly related with the vacancy of the frontier d-band state of d-metal.[73] It is posited that characteristics of the frontier d-band state in Pt can featured electrocatalytic activity for the ORR owing to control of adsorption strength of oxygen containing intermediate species such as O, OH and OOH, by smaller band width.[15] Hence, the Pt L_3 edge, transition from $2p_{3/2}$ to 5d band, offered qualitative information about the degree of d-band filling associated with the activity of electrocatalysts.[14, 59, 107] Intensities of the absorption edge of Pt L_3, were increased in a descending order; PtNi_Ar $\leq$ PtNi_H2 $\ll$ PtNi_Air. (Fig 3.33(a)) Because the oxidative species of Pt was largely inclined as shown in XRD spectra for PtNi_Air, the white line intensity give rise to the high value compared to others. Interestingly, in case of PtNi_Ar and PtNi_H2, trends of the d-band vacancy were somewhat questioning in accordance with reducing ability of gaseous atmosphere. This result can carefully interpret that the vacancy of frontier d-band states was altered by the interaction between Pt and Ni, i.e., the electron transition was more facilitated in argon rather in hydrogen atmosphere during heat treatment process. However, intensities of Ni K main edge, allowed transition from 1s to 4p, showed the different aspect compared to Pt L_3 edge; PtNi_H2 < PtNi_Ar $\ll$ PtNi_Air.

According to our previous findings, oxygen species coordinated with Pt were transported to nickel during the heat treatment.[108] Increases in Ni K main edge for PtNi_Ar, in this respect, plausibly argued that Ni species promoted electron transfer toward Pt when to take trends in Pt L_3 edge into account.

The XPS analysis was performed to clarify electronic effects of each electrocatalysts. As shown in Fig 3.33(b) and (c), core level states of Pt $4f_{7/2}$ were exhibited. The binding energy of Pt 4f states was varied with gaseous environments during the heat treatment. Alteration of binding energy of core states was accompanied with surface d-band states at transition metal surface,[103, 109-110] important in controlling intrinsic kinetics for the ORR as mentioned above. Moreover, it has been reported that the binding energy of Pt 4f was moved toward higher value in consequence with interaction between Pt and d-band metal, shown in both experimental and theoretical way.[104, 111] In this view point, the downshift of d-band states of Pt, beneficial for the ORR resulting from weakening the adsorption of intermediate species,[14-15, 17, 64] were simultaneously achieved by higher binding energy shifts in core electronic states. Changes in binding energy of our electrocatalysts matched this fashion considering activity for the ORR. The binding energy of $Pt4f_{7/2}$ was gradually increased in accordance with facile kinetics of the ORR; PtNi_Ar (71.5 eV) > PtNi_H2 (71.1 eV) > PtNi_Air (71.0 eV). Interestingly, the activity for the ORR was much more sensitive in the presence of specific anion adsorption, 0.1 M $HClO_4$ + 0.1 M H_3PO_4.(Fig. 3.33(c)) This is consistent with our recent

findings, that is, anion adsorption kinetics can be enhanced by tailoring the downshift of the d-band center.[112] It is, therefore, that the enhancement of the ORR was attained by tuning electronic structures during annealing process especially in argon atmosphere.

Table 3.7. Quantitative analysis of XPS spectra of Pt 4f and Ni 2p.

Area Ratio (%)	Pt 4f				Ni 2p			x^* (Pt_1Ni_x)
	Pt(0)	Pt(II)	Pt(IV)	Average Oxidation Number	Ni(0)	Ni(II)	Average Oxidation Number	
PtNi(40)_Ar	52.4	33.4	14.2	1.24	10.0	90.0	1.80	0.44
PtNi(40)_H2	56.6	23.9	19.5	1.26	11.6	88.4	1.77	0.45
PtNi(40)_Air	33.0	36.1	30.9	1.96	0.6	99.4	1.99	0.50

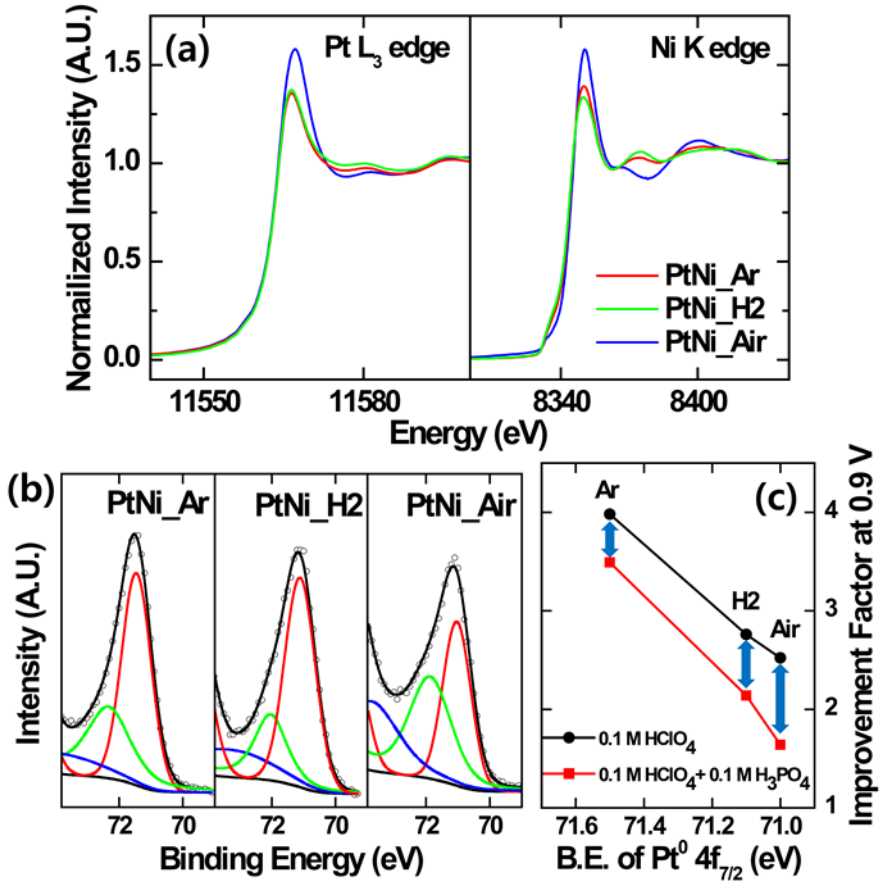

Figure 3.33. (a) XANES spectra of Pt L_3 edge and Ni K edge of PtNi nanoparticles, (b) XPS spectra of Pt $4f_{7/2}$, and (c) relation between binding energy and improvement factor.

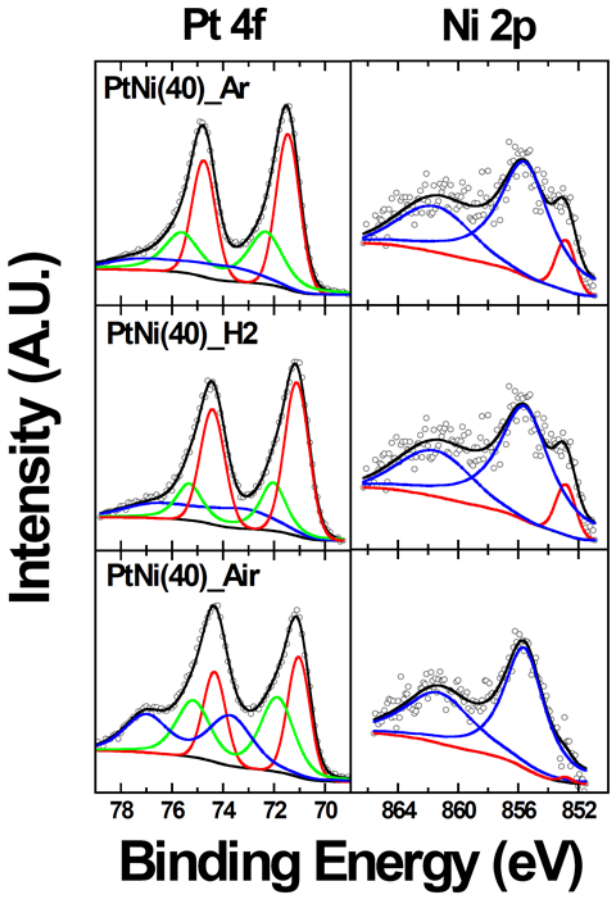

Figure 3.34. XPS spectra of Pt 4f and Ni 2p for PtNi nanoparticles.

Chapter 4. Conclusions

The electrochemistry in the ORR is decisively correlated with the electronic structure of Pt species. Due to the extremely large surface area, Pt-based nanoparticles were used as an electrocatalysts for the ORR. Pt-based nanoparticles were generally prepared via the wet chemical approach including colloidal reduction method with the surface adsorbed organic species. To utilize this nanoparticle as an electrocatalyst, many factors should be considered such as the preparation environment, the surface capped species, and the post-treatment process. In this thesis, it was investigated that the relationship between electrochemistry in the oxygen reduction and electronic structure for Pt-based nano-catalysts into the three categories, *i.e.*, preparation stage, as-prepared state, and post-treatment.

Firstly, we found that the relationship between the surface composition of Pt-based bimetallic nanoparticles and the electrocatalytic activity at the preparation stage. To clarify this relationship, we compared two types of nanoparticles with the different surface composition, *i.e.*, the Fe-rich and the Pt-Fe mixed surface. The carbon supported the Pt_1Fe_x (x = 1, 2, and 3) nanoparticles (~ 2 nm) with the Fe-rich surface were successfully prepared via the preferential interaction with Fe-OOC bonds, using a single capping agent, oleic acid. The nanoparticles with the Pt-Fe mixed surface were formed by the difference in the segregation energy, the heat treatment under the reductive atmosphere. The electrocatalytic activity was directly reflected by the surface composition of nanoparticles. This result could deepen

understanding of the relationship between the surface composition and the electrocatalytic activity of the Pt- based bimetallic nanoparticles

Secondly, the effect of surface capped species, oleylamine onto the surface of Pt nanoparticles, was studied at the as-prepared state. Organic molecule modified Pt nanoparticles featured a unique activity of ORRs. Despite a loss of the ESA, specific kinetic current density was over 3 times higher than that of the unmodified form. Coverage of surface covered organic species was directly related with downshift of ε_d relative to ε_F, similar to a most common strategy involving the introduction of other inorganic material. We also investigated the retardation of competitively adsorbed species by organically tailored surface at the different acidic electrolytes. It was confirmed that hindering spectator species lead to enhancement of ORR kinetics, and that this effect was more efficient in the presence of strong anion adsorption. The results support the idea that organic molecule capping electrocatalysts can improve reactivity by both electronic and structural modification.

Lastly, it was scrutinized how to affect the post-treatment, that is, thermal annealing of PtNi based nanoparticles with the different thermal energy and atmospheres. To elucidate the effect of thermal energy, we investigated how to affect intermetallic reconstruction of Pt-based bimetallic nanoparticles on the electrocatalytic activity. As thermal energy was introduced to the PtNi nanoparticles, structural reconstruction was carried out into the two features, *i.e.*, increasing intermetallic ordering and surface reorientation into the (111) facet. The reconstruction could be altered adsorption properties on the surface of nanoparticles, resulting in the high electrocatalytic activity of the

ORR compared to Pt nanoparticles. The intermetallic reconstructions give rise to forming the electrochemically stable structure and increasing intermetallic interaction by the characterization of PtNi nanoparticles after dissolution of Ni species during the electrochemical reaction. This result elucidated a point of contention how to achieve the enhancement the ORR activity of Pt-based nanoparticles through the thermal annealing process.

For investigation on the different atmosphere of thermal annealing, the carbon supported Pt_2Ni_1 nanoparticles were prepared via the colloidal method. The nanoparticles were heated under various gaseous atmospheres, such as argon, hydrogen. The structural characterization revealed that the particle size was ~ 3.5 nm and the alloyed phase was formed during heat treatment process despite the low crystallinity in case of PtNi_Air. The polarization curves of the ORR in 0.1 M $HClO_4$ and 0.1 M $HClO_4$ + 0.1 M H_3PO_4 were showed that the activity was varied with the treated gases, in the descending order, PtNi_Ar> PtNi_H2 >PtNi_Air. This result might be stem from the alteration of the electronic structure in accordance with X-ray spectroscopic techniques including XANES and XPS. Particularly, kinetics of the ORR was more sensitive to the shift of the electronic structure, when to measure the electrocatalytic properties in the presence of the specific anion adsorption.

References

(1) Wagner, F. T.; Lakshmanan, B.; Mathias, M. F. Electrochemistry and the Future of the Automobile. *J. Phys. Chem. Lett.* **2010,** *1,* 2204-2219.

(2) Wang, Y.; Chen, K. S.; Mishler, J.; Cho, S. C.; Adroher, X. C. A Review of Polymer Electrolyte Membrane Fuel Cells: Technology, Applications, and Needs on Fundamental Research. *Applied Energy* **2011,** *88,* 981-1007.

(3) The Fuel Cell Industry Review 2012. *Fuel Cell Today* 2012.

(4) Zhang, J., *Pem Fuel Cell Electrocatalysts and Catalyst Layers: Fundamentals and Applications*. Springer London, Limited: 2008.

(5) In *Doe Fuel Cell Technology Program Overview and Introduction to the 2010 Fuel Cell Pre-Solicitation Workshop in Doe Fuel Cell Pre-Solicitation Workshop*, Colorado, Department of Energy: Colorado, 2010.

(6) Hammer, B.; Nørskov, J. K. Theoretical Surface Science and Catalysis—Calculations and Concepts. *Adv. Catal.* **2000,** *45,* 71-129.

(7) Pettifor, D. G., *Bonding and Structure of Molecules and Solids*. Oxford University Press, Incorporated: 1995.

(8) Lambert, R. M.; Pacchioni, G.; Division, N. A. T. O. S. A., *Chemisorption and Reactivity on Supported Clusters and Thin Films: Towards an Understanding of Microscopic Processes in Catalysis*. Springer: 1997.

(9) Nørskov, J. K.; Bligaard, T.; Logadottir, A.; Bahn, S.; Hansen, L. B.; Bollinger, M.; Bengaard, H.; Hammer, B.; Sljivancanin, Z.; Mavrikakis, M.; Xu, Y.; Dahl, S.; Jacobsen, C. J. H. Universality in Heterogeneous Catalysis.

J. Catal. **2002,** *209,* 275-278.

(10) Bronsted, J. N. Acid and Basic Catalysis. *Chem. Rev.* **1928,** *5,* 231-338.

(11) Evans, M. G.; Polanyi, M. Inertia and Driving Force of Chemical Reactions. *Trans. Faraday Soc.* **1938,** *34,* 11-24.

(12) Nørskov, J. K.; Rossmeisl, J.; Logadottir, A.; Lindqvist, L.; Kitchin, J. R.; Bligaard, T.; Jónsson, H. Origin of the Overpotential for Oxygen Reduction at a Fuel-Cell Cathode. *J. Phys. Chem. B* **2004,** *108,* 17886-17892.

(13) Zhdanov, V. P.; Kasemo, B. Kinetics of Electrochemical O_2 Reduction on Pt. *Electrochem. Commun.* **2006,** *8,* 1132-1136.

(14) Stephens, I. E. L.; Bondarenko, A. S.; Gronbjerg, U.; Rossmeisl, J.; Chorkendorff, I. Understanding the Electrocatalysis of Oxygen Reduction on Platinum and Its Alloys. *Energy Environ. Sci.* **2012,** *5,* 6744-6762.

(15) Bligaard, T.; Nørskov, J. K. Ligand Effects in Heterogeneous Catalysis and Electrochemistry. *Electrochim. Acta* **2007,** *52,* 5512-5516.

(16) Hammer, B.; Nielsen, O. H.; Nrskov, J. K. Structure Sensitivity in Adsorption: Co Interaction with Stepped and Reconstructed Pt Surfaces. *Catal. Lett.* **1997,** *46,* 31-35.

(17) Kitchin, J. R.; Nørskov, J. K.; Barteau, M. A.; Chen, J. G. Modification of the Surface Electronic and Chemical Properties of Pt(111) by Subsurface 3d Transition Metals. *J. Chem. Phys.* **2004,** *120,* 10240-10246.

(18) Ruban, A.; Hammer, B.; Stoltze, P.; Skriver, H. L.; Nørskov, J. K. Surface Electronic Structure and Reactivity of Transition and Noble Metals. *J. Mol. Catal. A: Chem.* **1997,** *115,* 421-429.

(19) Zhang, J.; Vukmirovic, M. B.; Xu, Y.; Mavrikakis, M.; Adzic, R. R.

Controlling the Catalytic Activity of Platinum-Monolayer Electrocatalysts for Oxygen Reduction with Different Substrates. *Angew. Chem.* **2005,** *117,* 2170-2173.

(20) Stamenkovic, V. R.; Mun, B. S.; Arenz, M.; Mayrhofer, K. J. J.; Lucas, C. A.; Wang, G.; Ross, P. N.; Markovic, N. M. Trends in Electrocatalysis on Extended and Nanoscale Pt-Bimetallic Alloy Surfaces. *Nat. Mater.* **2007,** *6,* 241-247.

(21) Stamenkovic, V. R.; Fowler, B.; Mun, B. S.; Wang, G.; Ross, P. N.; Lucas, C. A.; Marković, N. M. Improved Oxygen Reduction Activity on $Pt_3Ni(111)$ via Increased Surface Site Availability. *Science* **2007,** *315,* 493-497.

(22) Tripkovic, D. V.; Strmcnik, D.; Van Der Vliet, D.; Stamenkovic, V.; Markovic, N. M. The Role of Anions in Surface Electrochemistry. *Faraday Discuss.* **2008,** *140,* 25-40.

(23) Schmidt, T. J.; Paulus, U. A.; Gasteiger, H. A.; Behm, R. J. The Oxygen Reduction Reaction on a Pt/Carbon Fuel Cell Catalyst in the Presence of Chloride Anions. *J. Electroanal. Chem.* **2001,** *508,* 41-47.

(24) Strmcnik, D. S.; Rebec, P.; Gaberscek, M.; Tripkovic, D.; Stamenkovic, V.; Lucas, C.; Marković, N. M. Relationship between the Surface Coverage of Spectator Species and the Rate of Electrocatalytic Reactions. *J. Phys. Chem. C* **2007,** *111,* 18672-18678.

(25) Gisbert, R.; García, G.; Koper, M. T. M. Adsorption of Phosphate Species on Poly-Oriented Pt and Pt(111) Electrodes over a Wide Range of Ph. *Electrochim. Acta* **2010,** *55,* 7961-7968.

(26) Strmcnik, D.; Escudero-Escribano, M.; Kodama, K.; Stamenkovic, V. R.; Cuesta, A.; Markovic, N. M. Enhanced Electrocatalysis of the Oxygen

Reduction Reaction Based on Patterning of Platinum Surfaces with Cyanide. *Nat. Chem.* **2010,** *2,* 880-885.

(27) Lee, K. S.; Yoo, S. J.; Ahn, D.; Kim, S. K.; Hwang, S. J.; Sung, Y. E.; Kim, H. J.; Cho, E.; Henkensmeier, D.; Lim, T. H.; Jang, J. H. Phosphate Adsorption and its Effect on Oxygen Reduction Reaction for Pt_xCo_y Alloy and Au_{core}-Pt_{shell} Electrocatalysts. *Electrochim. Acta* **2011,** *56,* 8802-8810.

(28) He, Q.; Shyam, B.; Nishijima, M.; Ramaker, D.; Mukerjee, S. Mitigating Phosphate Anion Poisoning of Cathodic Pt/C Catalysts in Phosphoric Acid Fuel Cells. *J. Phys. Chem. C* **2013,** *117,* 4877-4887.

(29) Lim, B.; Yu, T.; Xia, Y. Shaping a Bright Future for Platinum-Based Alloy Electrocatalysts. *Angew. Chem. Int. Ed.* **2010,** *49,* 9819-9820.

(30) Lamer, V. K.; Dinegar, R. H. Theory, Production and Mechanism of Formation of Monodispersed Hydrosols. *J. Am. Chem. Soc.* **1950,** *72,* 4847-4854.

(31) Murray, C. B.; Kagan, C. R.; Bawendi, M. G. Synthesis and Characterization of Monodisperse Nanocrystals and Close-Packed Nanocrystal Assemblies. *Annu. Rev. Mater. Sci.* **2000,** *30,* 545-610.

(32) Park, J.; Joo, J.; Soon, G. K.; Jang, Y.; Hyeon, T. Synthesis of Monodisperse Spherical Nanocrystals. *Angew. Chem. Int. Ed.* **2007,** *46,* 4630-4660.

(33) Peng, Z.; Yang, H. Designer Platinum Nanoparticles: Control of Shape, Composition in Alloy, Nanostructure and Electrocatalytic Property. *Nano Today* **2009,** *4,* 143-164.

(34) Li, D.; Wang, C.; Tripkovic, D.; Sun, S.; Markovic, N. M.; Stamenkovic, V. R. Surfactant Removal for Colloidal Nanoparticles from Solution

Synthesis: The Effect on Catalytic Performance. *ACS Catal.* **2012,** *2,* 1358-1362.

(35) Wang, C.; Daimon, H.; Lee, Y.; Kim, J.; Sun, S. Synthesis of Monodisperse Pt Nanocubes and Their Enhanced Catalysis for Oxygen Reduction. *J. Am. Chem. Soc.* **2007,** *129,* 6974-6975.

(36) Wu, B.; Zheng, N.; Fu, G. Small Molecules Control the Formation of Pt Nanocrystals: A Key Role of Carbon Monoxide in the Synthesis of Pt Nanocubes. *Chem. Commun.* **2011,** *47,* 1039-1041.

(37) Zhang, J.; Fang, J. A General Strategy for Preparation of Pt 3d-Transition Metal (Co, Fe, Ni) Nanocubes. *J. Am. Chem. Soc.* **2009,** *131,* 18543-18547.

(38) Lai, F.-J.; Chou, H.-L.; Sarma, L. S.; Wang, D.-Y.; Lin, Y.-C.; Lee, J.-F.; Hwang, B.-J.; Chen, C.-C. Tunable Properties of Pt_xFe_{1-X} Electrocatalysts and Their Catalytic Activity Towards the Oxygen Reduction Reaction. *Nanoscale* **2010,** *2,* 573-581.

(39) Wang, C.; Chi, M.; Li, D.; van der Vliet, D.; Wang, G.; Lin, Q.; F. Mitchell, J.; More, K. L.; Markovic, N. M.; Stamenkovic, V. R. Synthesis of Homogeneous Pt-Bimetallic Nanoparticles as Highly Efficient Electrocatalysts. *ACS Catal.* **2011,** *1,* 1355-1359.

(40) Wang, C.; Chi, M.; Wang, G.; Van Der Vliet, D.; Li, D.; More, K.; Wang, H. H.; Schlueter, J. A.; Markovic, N. M.; Stamenkovic, V. R. Correlation between Surface Chemistry and Electrocatalytic Properties of Monodisperse Pt_XNi_{1-X} Nanoparticles. *Adv. Funct. Mater.* **2011,** *21,* 147-152.

(41) Zhang, J.; Yang, H.; Yang, K.; Fang, J.; Zou, S.; Luo, Z.; Wang, H.; Bae, I.-T.; Jung, D. Y. Monodisperse Pt_3Fe Nanocubes: Synthesis, Characterization, Self-Assembly, and Electrocatalytic Activity. *Adv. Funct.*

Mater. **2010,** *20,* 3727-3733.

(42) Malheiro, A. R.; Perez, J.; Villullas, H. M. Well-Alloyed Ptfec Nanocatalysts of Controlled Composition and Same Particle Size: Oxygen Reduction and Methanol Tolerance. *J. Electrochem. Soc.* **2009,** *156,* B51-B58.

(43) Ritz, B.; Heller, H.; Myalitsin, A.; Kornowski, A.; Martin-Martinez, F. J.; Melchor, S.; Dobado, J. A.; Juárez, B. H.; Weller, H.; Klinke, C. Reversible Attachment of Platinum Alloy Nanoparticles to Nonfunctionalized Carbon Nanotubes. *ACS Nano* **2010,** *4,* 2438-2444.

(44) Cushing, B. L.; Kolesnichenko, V. L.; O'Connor, C. J. Recent Advances in the Liquid-Phase Syntheses of Inorganic Nanoparticles. *Chem. Rev.* **2004,** *104,* 3893-3946.

(45) de la Presa, P.; Rueda, T.; Hernando, A.; Ramallo-Lopez, J. M.; Giovanetti, L. J.; Requejo, F. G. Spontaneous Oxidation of Disordered Fcc FePt Nanoparticles. *J. Appl. Phys.* **2008,** *103,* 103909-8.

(46) Shukla, N.; Liu, C.; Jones, P. M.; Weller, D. Ftir Study of Surfactant Bonding to FePt Nanoparticles. *J. Magn. Magn. Mater.* **2003,** *266,* 178-184.

(47) Sun, S.; Anders, S.; Thomson, T.; Baglin, J. E. E.; Toney, M. F.; Hamann, H. F.; Murray, C. B.; Terris, B. D. Controlled Synthesis and Assembly of FePt Nanoparticles. *J. Phys. Chem. B* **2003,** *107,* 5419-5425.

(48) Figueroa, S. J. A.; Stewart, S. J.; Rueda, T.; Hernando, A.; de la Presa, P. Thermal Evolution of Pt-Rich FePt/Fe_3O_4 Heterodimers Studied Using X-Ray Absorption near-Edge Spectroscopy. *J. Phys. Chem. C* **2011,** *115,* 5500-5508.

(49) Zhao, F.; Rutherford, M.; Grisham, S. Y.; Peng, X. Formation of

Monodisperse FePt Alloy Nanocrystals Using Air-Stable Precursors: Fatty Acids as Alloying Mediator and Reductant for Fe3+ Precursors. *J. Am. Chem. Soc.* **2009,** *131,* 5350-5358.

(50) Kang, Y.; Murray, C. B. Synthesis and Electrocatalytic Properties of Cubic Mn-Pt Nanocrystals (Nanocubes). *J. Am. Chem. Soc.* **2010,** *132,* 7568-7569.

(51) Li, W.; Chen, Z.; Xu, L.; Yan, Y. A Solution-Phase Synthesis Method to Highly Active Pt-Co/C Electrocatalysts for Proton Exchange Membrane Fuel Cell. *J. Power Sources* **2010,** *195,* 2534-2540.

(52) Lee, Y. H.; Lee, G.; Shim, J. H.; Hwang, S.; Kwak, J.; Lee, K.; Song, H.; Park, J. T. Monodisperse PtRu Nanoalloy on Carbon as a High-Performance DMFC Catalyst. *Chem. Mater.* **2006,** *18,* 4209-4211.

(53) Mazumder, V.; Sun, S. Oleylamine-Mediated Synthesis of Pd Nanoparticles for Catalytic Formic Acid Oxidation. *J. Am. Chem. Soc.* **2009,** *131,* 4588-4589.

(54) Delalande, M.; Marcoux, P. R.; Reiss, P.; Samson, Y. Core-Shell Structure of Chemically Synthesised Fept Nanoparticles: A Comparative Study. *J. Mater. Chem.* **2007,** *17,* 1579-1588.

(55) Dey, R.; Mukherjee, N.; Ahammed, S.; Ranu, B. C. Highly Selective Reduction of Nitroarenes by Iron(0) Nanoparticles in Water. *Chem. Commun.* **2012,** *48,* 7982-7984.

(56) Christensen, A.; Ruban, A. V.; Stoltze, P.; Jacobsen, K. W.; Skriver, H. L.; Nørskov, J. K.; Besenbacher, F. Phase Diagrams for Surface Alloys. *Phys. Rev. B* **1997,** *56,* 5822-5834.

(57) Ruban, A. V.; Skriver, H. L.; Nørskov, J. K. Surface Segregation

Energies in Transition-Metal Alloys. *Phys. Rev. B* **1999,** *59,* 15990-16000.

(58) Nguyen, H. L.; Howard, L. E. M.; Stinton, G. W.; Giblin, S. R.; Tanner, B. K.; Terry, I.; Hughes, A. K.; Ross, I. M.; Serres, A.; Evans, J. S. O. Synthesis of Size-Controlled fcc and fct FePt Nanoparticles. *Chem. Mater.* **2006,** *18,* 6414-6424.

(59) Mansour, A. N.; Cook, J. W.; Sayers, D. E. Quantitative Technique for the Determination of the Number of Unoccupied d-Electron States in a Platinum Catalyst Using the $L_{2,3}$ X-Ray Absorption Edge Spectra. *J. Phys. Chem.* **1984,** *88,* 2330-2334.

(60) Russell, A. E.; Maniguet, S.; Mathew, R. J.; Yao, J.; Roberts, M. A.; Thompsett, D. In Situ X-Ray Absorption Spectroscopy and X-Ray Diffraction of Fuel Cell Electrocatalysts. *J. Power Sources* **2001,** *96,* 226-232.

(61) Lai, F.-J.; Sarma, L. S.; Chou, H.-L.; Liu, D.-G.; Hsieh, C.-A.; Lee, J.-F.; Hwang, B.-J. Architecture of Bimetallic Pt_xCo_{1-X} Electrocatalysts for Oxygen Reduction Reaction as Investigated by X-Ray Absorption Spectroscopy. *J. Phys. Chem. C* **2009,** *113,* 12674-12681.

(62) van der Vliet, D. F.; Wang, C.; Li, D.; Paulikas, A. P.; Greeley, J.; Rankin, R. B.; Strmcnik, D.; Tripkovic, D.; Markovic, N. M.; Stamenkovic, V. R. Unique Electrochemical Adsorption Properties of Pt-Skin Surfaces. *Angew. Chem. Int. Ed.* **2012,** *51,* 3139-3142.

(63) Urchaga, P.; Baranton, S.; Coutanceau, C.; Jerkiewicz, G. Electro-Oxidation of CO_{chem} on Pt Nanosurfaces: Solution of the Peak Multiplicity Puzzle. *Langmuir* **2011,** *28,* 3658-3663.

(64) Nørskov, J. K.; Rossmeisl, J.; Logadottir, A.; Lindqvist, L.; Kitchin, J. R.; Bligaard, T.; Jónsson, H. Origin of the Overpotential for Oxygen

Reduction at a Fuel-Cell Cathode. *J. Phys. Chem. B* **2004,** *108,* 17886-17892.

(65) Gan, L.; Heggen, M.; Rudi, S.; Strasser, P. Core–Shell Compositional Fine Structures of Dealloyed Pt_xNi_{1-x} Nanoparticles and Their Impact on Oxygen Reduction Catalysis. *Nano Lett.* **2012,** *12,* 5423-5430.

(66) Kanezashi, I.; Nohara, S.; Omura, J.; Watanabe, M.; Uchida, H. Electrochemical Quartz Crystal Microbalance Analysis of the CO Oxidation Reaction at Pt Alloy Electrodes. *J. Electroanal. Chem.* **2011,** *662,* 123-129.

(67) Jeon, T.-Y.; Pinna, N.; Yoo, S. J.; Yu, S.-H.; Kim, S.-K.; Lim, S.; Peck, D.; Jung, D.-H.; Sung, Y.-E. Enhanced Activity of Pt-Based Electrocatalysts for Oxygen Reduction Via a Selective Pt Deposition Process. *J. Electroanal. Chem.* **2011,** *662,* 70-79.

(68) Hammer, B.; Nørskov, J. K., Theoretical Surface Science and Catalysis—Calculations and Concepts. In *Adv. Catal.*, Bruce C. Gates, H. K., Ed. Academic Press: 2000; Vol. Volume 45, pp 71-129.

(69) Mun, B. S.; Lee, C.; Stamenkovic, V.; Markovic, N. M.; Ross, P. N. Electronic Structure of Pd Thin Films on Re(0001) Studied by High-Resolution Core-Level and Valence-Band Photoemission. *Phys. Rev. B* **2005,** *71,* 115420.

(70) Zhou, W. P.; Lewera, A.; Larsen, R.; Masel, R. I.; Bagus, P. S.; Wieckowski, A. Size Effects in Electronic and Catalytic Properties of Unsupported Palladium Nanoparticles in Electrooxidation of Formic Acid. *J. Phys. Chem. B* **2006,** *110,* 13393-13398.

(71) Yoo, S. J.; Kim, S.-K.; Jeon, T.-Y.; Hwang, S. J.; Lee, J.-G.; Lee, S.-C.; Lee, K.-S.; Cho, Y.-H.; Sung, Y.-E.; Lim, T.-H. Enhanced Stability and Activity of Pt-Y Alloy Catalysts for Electrocatalytic Oxygen Reduction. *Chem. Commun.* **2011,** *47,* 11414-11416.

(72) Stamenkovic, V.; Mun, B. S.; Mayrhofer, K. J. J.; Ross, P. N.; Markovic, N. M.; Rossmeisl, J.; Greeley, J.; Nørskov, J. K. Changing the Activity of Electrocatalysts for Oxygen Reduction by Tuning the Surface Electronic Structure. *Angew. Chem. Int. Ed.* **2006,** *45,* 2897-2901.

(73) Russell, A. E.; Rose, A. X-Ray Absorption Spectroscopy of Low Temperature Fuel Cell Catalysts. *Chem. Rev.* **2004,** *104,* 4613-4636.

(74) Mukerjee, S.; Srinivasan, S.; Soriaga, M. P.; McBreen, J. Role of Structural and Electronic-Properties of Pt and Pt Alloys on Electrocatalysis of Oxygen Reduction - an *in-situ* XANES and EXAFS Investigation. *J. Electrochem. Soc.* **1995,** *142,* 1409-1422.

(75) Qiu, L.; Liu, F.; Zhao, L.; Yang, W.; Yao, J. Evidence of a Unique Electron Donor−Acceptor Property for Platinum Nanoparticles as Studied by XPS. *Langmuir* **2006,** *22,* 4480-4482.

(76) Sabatier, P. Hydrogénations Et Déshydrogénations Par Catalyse. *Ber. Deutsch. Chem. Gesellschaft* **1911,** *44,* 1984-2001.

(77) Wang, J. X.; Markovic, N. M.; Adzic, R. R. Kinetic Analysis of Oxygen Reduction on Pt(111) in Acid Solutions: Intrinsic Kinetic Parameters and Anion Adsorption Effects. *J. Phys. Chem. B* **2004,** *108,* 4127-4133.

(78) Hsueh, K. L.; Gonzalez, E. R.; Srinivasan, S. Effects of Phosphoric Acid Concentration on Oxygen Reduction Kinetics at Platinum. *J. Electrochem. Soc.* **1984,** *131,* 823-828.

(79) Lee, K. S.; Yoo, S. J.; Ahn, D.; Kim, S. K.; Hwang, S. J.; Sung, Y.-E.; Kim, H. J.; Cho, E.; Henkensmeier, D.; Lim, T. H.; Jang, J. H. Phosphate Adsorption and Its Effect on Oxygen Reduction Reaction for Ptxcoy Alloy and Au_{core}-Pt_{shell} Electrocatalysts. *Electrochim. Acta* **2011,** *56,* 8802-8810.

(80) Mostany, J.; Martínez, P.; Climent, V.; Herrero, E.; Feliu, J. M. Thermodynamic Studies of Phosphate Adsorption on Pt(111) Electrode Surfaces in Perchloric Acid Solutions. *Electrochim. Acta* **2009,** *54,* 5836-5843.

(81) Ross, P. N.; Andricacos, P. C. The Effect of $H_2PO_4^-$ Anion on the Kinetics of Oxygen Reduction on Pt. *J. Electroanal. Chem.* **1983,** *154,* 205-215.

(82) He, Q.; Yang, X.; Chen, W.; Mukerjee, S.; Koel, B.; Chen, S. Influence of Phosphate Anion Adsorption on the Kinetics of Oxygen Electroreduction on Low Index Pt(hkl) Single Crystals. *Phys. Chem. Chem. Phys.* **2010,** *12,* 12544-12555.

(83) GreeleyJ; Stephens, I. E. L.; Bondarenko, A. S.; Johansson, T. P.; Hansen, H. A.; Jaramillo, T. F.; RossmeislJ; ChorkendorffI; Nørskov, J. K. Alloys of Platinum and Early Transition Metals as Oxygen Reduction Electrocatalysts. *Nat. Chem.* **2009,** *1,* 552-556.

(84) Hwang, S. J.; Kim, S.-K.; Lee, J.-G.; Lee, S.-C.; Jang, J. H.; Kim, P.; Lim, T.-H.; Sung, Y.-E.; Yoo, S. J. Role of Electronic Perturbation in Stability and Activity of Pt-Based Alloy Nanocatalysts for Oxygen Reduction. *J. Am. Chem. Soc.* **2012,** *134,* 19508-19511.

(85) Xia, Y.; Xiong, Y.; Lim, B.; Skrabalak, S. E. Shape-Controlled Synthesis of Metal Nanocrystals: Simple Chemistry Meets Complex Physics? *Angew. Chem. Int. Ed.* **2009,** *48,* 60-103.

(86) Sun, S.; Zhang, G.; Geng, D.; Chen, Y.; Li, R.; Cai, M.; Sun, X. A Highly Durable Platinum Nanocatalyst for Proton Exchange Membrane Fuel Cells: Multiarmed Starlike Nanowire Single Crystal. *Angew. Chem. Int. Ed.* **2011,** *50,* 422-426.

(87) Wang, C.; Chi, M.; Li, D.; Strmcnik, D.; van der Vliet, D.; Wang, G.; Komanicky, V.; Chang, K.-C.; Paulikas, A. P.; Tripkovic, D.; Pearson, J.; More, K. L.; Markovic, N. M.; Stamenkovic, V. R. Design and Synthesis of Bimetallic Electrocatalyst with Multilayered Pt-Skin Surfaces. *J. Am. Chem. Soc.* **2011,** *133,* 14396-14403.

(88) van der Vliet, D. F.; Wang, C.; Tripkovic, D.; Strmcnik, D.; Zhang, X. F.; Debe, M. K.; Atanasoski, R. T.; Markovic, N. M.; Stamenkovic, V. R. Mesostructured Thin Films as Electrocatalysts with Tunable Composition and Surface Morphology. *Nat Mater* **2012,** *11,* 1051-1058.

(89) Hansen, M.; Anderko, K., *Constitution of Binary Alloys*. McGraw-Hill: 1965.

(90) Leroux, C.; Cadeville, M. C.; Pierron-Bohnes, V.; Inden, G.; Hinz, F. Comparative Investigation of Structural and Transport Properties of $L1_0$ NiPt and CoPt Phases; the Role of Magnetism. *J. Phys. F* **1988,** *18,* 2033-2051.

(91) Xiong, L.; Manthiram, A. Effect of Atomic Ordering on the Catalytic Activity of Carbon Supported Ptm (M = Fe, Co, Ni, and Cu) Alloys for Oxygen Reduction in Pemfcs. *J. Electrochem. Soc.* **2005,** *152,* A697-A703.

(92) Schroeder, R. H.; Schmitz-Pranghe, N.; Kohlhaas, R. Experimental Determination of the Lattice Parameters of Platinum Metals at -190 to 1709 ^{O}C Right Bracket. *Zeitschrift fur Metallkunde* **1972,** *63,* 12-16.

(93) Patterson, A. L. The Scherrer Formula for X-Ray Particle Size Determination. *Phys. Rev.* **1939,** *56,* 978-982.

(94) Koper, M. T. M. Structure Sensitivity and Nanoscale Effects in Electrocatalysis. *Nanoscale* **2011,** *3,* 2054-2073.

(95) Brimaud, S.; Pronier, S.; Coutanceau, C.; Léger, J. M. New Findings on

CO Electrooxidation at Platinum Nanoparticle Surfaces. *Electrochem. Commun.* **2008,** *10,* 1703-1707.

(96) Clavilier, J.; Feliu, J. M.; Aldaz, A. An Irreversible Structure Sensitive Adsorption Step in Bismuth Underpotential Deposition at Platinum Electrodes. *J. Electroanal. Chem.* **1988,** *243,* 419-433.

(97) Rodríguez, P.; Solla-Gullón, J.; Vidal-Iglesias, F. J.; Herrero, E.; Aldaz, A.; Feliu, J. M. Determination of (111) Ordered Domains on Platinum Electrodes by Irreversible Adsorption of Bismuth. *Anal. Chem.* **2005,** *77,* 5317-5323.

(98) Rodríguez, P.; Herrero, E.; Solla-Gullón, J.; Vidal-Iglesias, F. J.; Aldaz, A.; Feliu, J. M. Specific Surface Reactions for Identification of Platinum Surface Domains: Surface Characterization and Electrocatalytic Tests. *Electrochim. Acta* **2005,** *50,* 4308-4317.

(99) Schmidt, T. J.; Grgur, B. N.; Behm, R. J.; Markovic, N. M.; Ross P.N, Jr. Bi Adsorption on Pt(111) in Perchloric Acid Solution: A Rotating Ring - Disk Electrode and Xps Study. *Phys. Chem. Chem. Phys.* **2000,** *2,* 4379-4386.

(100) Stamenkovic, V. R.; Fowler, B.; Mun, B. S.; Wang, G.; Ross, P. N.; Lucas, C. A.; Markovic, N. M. Improved Oxygen Reduction Activity on $Pt_3Ni(111)$ via Increased Surface Site Availability. *Science* **2007,** *315,* 493-497.

(101) Stamenkovic, V. R.; Mun, B. S.; Mayrhofer, K. J. J.; Ross, P. N.; Markovic, N. M. Effect of Surface Composition on Electronic Structure, Stability, and Electrocatalytic Properties of Pt-Transition Metal Alloys: Pt-Skin Versus Pt-Skeleton Surfaces. *J. Am. Chem. Soc.* **2006,** *128,* 8813-8819.

(102) Ganduglia-Pirovano, M. V.; Natoli, V.; Cohen, M. H.; Kudrnovský, J.;

Turek, I. Potential, Core-Level, and d Band Shifts at Transition-Metal Surfaces. *Phys. Rev. B* **1996,** *54,* 8892-8898.

(103) Weinert, M.; Watson, R. E. Core-Level Shifts in Bulk Alloys and Surface Adlayers. *Phys. Rev. B* **1995,** *51,* 17168-17180.

(104) Toyoda, E.; Jinnouchi, R.; Ohsuna, T.; Hatanaka, T.; Aizawa, T.; Otani, S.; Kido, Y.; Morimoto, Y. Catalytic Activity of Pt/TaB_2(0001) for the Oxygen Reduction Reaction. *Angew. Chem. Int. Ed.* **2013,** *52,* 4137-4140.

(105) Siegel, S.; Hoekstra, H. R.; Tani, B. S. The Crystal Structure of Beta-Platinum Dioxide. *J. Inorg. Nucl. Chem.* **1969,** *31,* 3803-3807.

(106) Kawahara, M.; Morita, J.; Rikukawa, M.; Sanui, K.; Ogata, N. Synthesis and Proton Conductivity of Thermally Stable Polymer Electrolyte: Poly(Benzimidazole) Complexes with Strong Acid Molecules. *Electrochim. Acta* **2000,** *45,* 1395-1398.

(107) Yoo, S. J.; Hwang, S. J.; Lee, J.-G.; Lee, S.-C.; Lim, T.-H.; Sung, Y.-E.; Wieckowski, A.; Kim, S.-K. Promoting Effects of La for Improved Oxygen Reduction Activity and High Stability of Pt on Pt-La Alloy Electrodes. *Energy Environ. Sci.* **2012,** *5,* 7521-7525.

(108) Jeon, T. Y.; Yoo, S. J.; Cho, Y. H.; Lee, K. S.; Kang, S. H.; Sung, Y.-E. Influence of Oxide on the Oxygen Reduction Reaction of Carbon-Supported Pt-Ni Alloy Nanoparticles. *J. Phys. Chem. C* **2009,** *113,* 19732-19739.

(109) Ganduglia-Pirovano, M. V.; Natoli, V.; Cohen, M. H.; Kudrnovský, J.; Turek, I. Potential, Core-Level, and d Band Shifts at Transition-Metal Surfaces. *Phys. Rev. B* **1996,** *54,* 8892-8898.

(110) Hennig, D.; Ganduglia-Pirovano, M. V.; Scheffler, M. Adlayer Core-Level Shifts of Admetal Monolayers on Transition-Metal Substrates and

Their Relation to the Surface Chemical Reactivity. *Phys. Rev. B* **1996,** *53,* 10344-10347.

(111) Toda, T.; Igarashi, H.; Uchida, H.; Watanabe, M. Enhancement of the Electroreduction of Oxygen on Pt Alloys with Fe, Ni, and Co. *J. Electrochem. Soc.* **1999,** *146,* 3750-3756.

(112) Chung, Y.-H.; Chung, D. Y.; Jung, N.; Sung, Y.-E. Tailoring the Electronic Structure of Nanoelectrocatalysts Induced by a Surface-Capping Organic Molecule for the Oxygen Reduction Reaction. *J. Phys. Chem. Lett.* **2013,** *4,* 1304-1309.

국 문 초 록

화학적 방법으로 준비된 백금 기반 나노입자에 대한 산소환원의 전기화학

수소이온 교환막 연료전지는 자동차와 휴대용 기기를 화석연료를 대체할 지속 가능한 에너지원으로서 각광받고 있다. 가장 높은 산소환원반응을 갖는 것으로 알려져 있는 백금 촉매는 그 높은 과전압 발생으로 인하여 수소이온 교환막 연료전지의 상용화를 저해하는 가장 큰 저해 요인으로 작용하고 있다. 이론에 의하면 백금(111)면과 산소를 포함하는 흡착종의 과도한 흡착 세기와 관련이 있다고 한다. 그 결과, 표면의 d-band 구조를 변화시켜 백금으로의 흡착 세기를 줄여 활성을 증대하기 위한 많은 노력들이 진행되고 있다.

지난 수 십 년 간, 백금 기반 촉매의 실질적인 적용을 위하여 카본 담지된 나노입자가 연구가 되고 있다. 나노입자를 얻기 위해서는 전구체로부터 생성된 핵이 느리게 자라나야 한다. 만약 성장 속도가 제어되지 않는다면 Ostwald ripening에 의하여 큰 입자가 형성되게 되어 입자 크기의 분포도가 증가하게 된다. 유기 용매, 캡

핑제, 환원제를 포함하는 합성 환경은 입체적, 정전기적 안정화를 통하여 성장 속도를 낮춰 나노입자의 표면을 안정화 시킬 수 있다. 그러나 사용된 유기종은 백금 기반 나노입자의 표면에 흡착하여 전기화학반응을 변화시킨다. 산소환원반응이 전자구조의 영향을 받는다는 것을 고려한다면 이를 변화시키는 합성단계, 준비된 상태, 사후 처리 과정과 같은 합성 환경이 매우 중요한 요소가 된다. 따라서 본 학위논문에서는 이 요소들에 따라 화학적 방법으로 준비된 백금 기반의 나노입자의 산소환원의 전기화학에 대해서 논하고자 한다.

백금 기반 나노 촉매의 준비 단계에 있어서 Pt_1Fe_x (x = 1, 2, 3) 나노입자를 연구하였다. 이 부분에서는 표면 조성이 전기화학 활성에 미치는 영향에 대한 이해를 목표로 한다. 이 관계를 명확히 하기 위하여 다른 표면 조성을 가진 두 가지 종류의 나노입자를 비교하였다. 캡핑제와 금속종의 선택적인 상호작용 (Fe−OOC)을 이용하여 약 2 nm의 고분산된 표면에 철이 존재하는 Pt_1Fe_x 나노입자를 합성하였다. 백금와 철의 비율이 달라짐에도 불구하고, 상 분리로 말미암아 전기화학 특성에 큰 변화가 관찰되지 않았다. 반면, 분리 에너지의 차이를 통하여 형성된 백금−철과 혼합된 표면의 경우 전기화학반응이 크게 변하는 것을 확인할 수 있었다. 특히 산소환원반응에 있어서 백금−철이 혼합된 표면을 가진 Pt_1Fe_2 나노입

자가 높은 활성을 갖는데 이는 안정된 백금-철 면심입방구조를 형성하였기 때문이다. 이 결과는 이종 금속 나노입자의 촉매 활성이 벌크 조성보다는 표면 조성에 의하여 결정된다는 것을 알려준다.

다음으로 나노촉매의 준비된 상태에 대하여 연구가 진행되었다. 백금 나노입자에 강하게 흡착하는 올레일아민을 포함한 유기 분자는 전기화학적 활성면적을 감소시키기 때문에 일반적으로 제거해야 할 것으로 여겨진다. 그러나 전기화학 활성 면적이 감소함에도 불구하고 올레일아민이 흡착된 백금 나노 입자가 산소환원반응의 활성을 증대시킨다는 것을 발견하였다. 이러한 활성 증가는 d-band 구조의 하향과 경쟁 흡착종의 지연에 기인하는 것과 관련이 있음을 확인하였다. 이 결과는 전극 표면에 흠착된 유기분자가 전자구조를 변화시켜 진보된 촉매를 설계하는 한 전략임을 알려준다.

마지막으로 PtNi 나노입자의 열처리를 통한 후처리 과정에 있어 온도와 분위기가 어떻게 영향을 주는 지에 대하여 알아보았다. 먼저 열처리 온도가 어떻게 산소환원반응에 영향을 미치는 지에 대해 탐구하였다. 합금의 정렬과 (111)면으로의 재배열과 같은 나노입자의 재구성이 다른 온도에서의 열처리를 통하여 큰 크기 변화 없이 이루어졌다. 전기화학 활성의 증가는 이러한 구조 변화와 관련이 있었다. 또한 전기화학적으로 안정한 구조가 형성되어 백금과 니켈의 상호작용이 증대하였다. 이러한 결과를 통하여 어떤 과정을

거쳐 열처리를 통하여 산소환원반응의 활성이 증대하는 지에 대해 알 수 있다. 두 번 째로 열처리 분위기에 따라 Pt_2Ni_1 나노입자의 산소환원반응이 변화되는 지에 대해 연구하였다. X선 분광 실험을 통하여 열처리 조건에 따라 전자구조가 바뀜을 확인하였다. 아르곤 처리된 촉매가 가장 높은 활성을 보였는데 이는 백금과 니켈의 전자적 적절한 상호작용에 기인한다. 이 결과는 열처리 분위기에 따른 전자구조의 변화가 산소환원반응에 결정적인 영향을 준다는 것을 확인 할 수 있었다.

주요어: 전기화학, 전자구조, 연료전지, 나노입자, 산소환원, 백금
학 번: 2009-31265